applied sciences

MDPI

Article

Three-Dimensional Distributions of the Direct Effect of anExtended and Intense Dust Aerosol Episode (16–18 June 2016) over the Mediterranean Basin on Regional Shortwave Radiation, Atmospheric Thermal Structure, and Dynamics

Maria Gavrouzou [1], Nikos Hatzianastassiou [1,*], Marios-Bruno Korras-Carraca [1,2], Michalis Stamatis [1], Christos Lolis [1], Christos Matsoukas [3], Nikos Michalopoulos [4,5] and Ilias Vardavas [6]

[1] Laboratory of Meteorology and Climatology, Department of Physics, University of Ioannina, 45110 Ioannina, Greece; m.gavrouzou@uoi.gr (M.G.); koras@env.aegean.gr (M.-B.K.-C.); m.stamatis@uoi.gr (M.S.); chlolis@uoi.gr (C.L.)
[2] Institute for Astronomy, Astrophysics, Space Applications and Remote Sensing, National Observatory of Athens, 15236 Athens, Greece
[3] Department of Environment, University of the Aegean, 81100 Mytilene, Greece; matsoukas@aegean.gr
[4] Institute for Environmental Research and Sustainable Development (IERSD), National Observatory of Athens, 15236 Athens, Greece; nmihalo@noa.gr
[5] Environmental Chemical Processes Laboratory, Department of Chemistry, University of Crete, 71500 Heraklion, Greece
[6] Department of Physics, University of Crete, 70013 Heraklion, Greece; vardavas@uoc.gr
* Correspondence: nhatzian@uoi.gr

Citation: Gavrouzou, M.; Hatzianastassiou, N.; Korras-Carraca, M.-B.; Stamatis, M.; Lolis, C.; Matsoukas, C.; Michalopoulos, N.; Vardavas, I. Three-Dimensional Distributions of the Direct Effect of anExtended and Intense Dust Aerosol Episode (16–18 June 2016) over the Mediterranean Basin on Regional Shortwave Radiation, Atmospheric Thermal Structure, and Dynamics. *Appl. Sci.* **2023**, *13*, 6878. https://doi.org/10.3390/app13126878

Academic Editors: Min-Suk Bae and Jane J. Liu

Received: 7 April 2023
Revised: 23 May 2023
Accepted: 2 June 2023
Published: 6 June 2023

Abstract: In the present study, we used the FORTH deterministic spectral Radiation Transfer Model (RTM) to estimate detailed three-dimensional distributions of the Direct Radiative Effects (DREs) and their consequent modification of the thermal structure of the regional atmosphere during an intense dust episode that took place from 16 to 18 June 2016 over the Mediterranean Basin (MB). The RTM operated on a 3-hourly temporal and 0.5 × 0.625° spatial resolution, using 3-D aerosol optical properties (i.e., aerosol optical depth, single scattering albedo, and asymmetry parameter) and other surface and atmospheric properties from the MERRA-2 reanalysis and cloud properties (i.e., cloud amount, cloud optical depth, and cloud top height) from the ISCCP-H dataset. The model ran with and without dust aerosols, yielding the upwelling and downwelling solar fluxes at the top of the atmosphere, in the atmosphere, and at the Earth's surface as well as at 50 levels in the atmosphere. The dust direct radiative effect (DDRE) was estimated as the difference between the two (one taking into account all aerosol types and one taking into account all except for dust aerosols) flux outputs. The atmospheric heating rates and subsequent convection induced by dust radiative absorption were calculated at 50 levels to determine how the DDRE affects the thermal structure and dynamics of the atmosphere. The results showed that such a great and intense dust transport event significantly reduces the net surface solar radiation over the MB (by up to 62 W/m^2 on a daily mean basis, and up to 200 W/m^2 on an hourly basis, at 12:00 UTC) while increasing the atmospheric solar absorption (by up to 72 W/m^2 daily and 187 W/m^2 hourly, at 12:00 UTC). At the top of the atmosphere, both heating (over desert areas) and cooling (over oceanic and other continental areas) are observed due to the significantly different surface albedos. Transported dust causes considerable heating of the region's atmosphere, which becomes maximum at altitudes where the dust loadings are highest (0.14 K/3 h on 17 June 2016, 12:00 UTC, at 3–5 km above sea level). The dust solar absorption and heating induce a buoyancy as strong as 0.014 m/s^2, resulting in considerable changes in vertical air motions and possibly contributing to the formation of middle- and high-level clouds over the Mediterranean Basin.

Keywords: dust episodes; Mediterranean Basin; radiative forcing; heating rates; buoyancy

1. Introduction

Dust Aerosols (DAs) are very important, since they largely contribute to the global aerosol mass in the atmosphere by more than 50% [1,2]. They perturb the Earth's radiation budget through their direct interaction with solar and terrestrial radiation, but also indirectly through modification of the cloud properties. Specifically, DAs absorb and scatter the shortwave radiation [3] and absorb and re-emit longwave radiation [4]. The interaction of DAs with SW radiation results in a positive anomaly of the atmospheric absorbed solar radiation (atmospheric heating effect) and a (greater over most regions) negative anomaly of the net surface solar radiation (surface cooling effect). The sum of these two opposite-sign effects results in an overall cooling effect of Dust Radiation Interaction (DRI) at the Top of Atmosphere (TOA), which is estimated to be equal to -0.83 W/m^2 on a climatological (for the years 1980–2018) annual global mean basis, arising from global mean surface cooling and atmospheric heating radiative effects equal to -1.98 W/m^2 and 1.15 W/m^2, respectively [5]. The annual mean SW Dust Direct Radiative Effects (DDREs) are greater over regions with high dust loads, namely world deserts, and especially the Sahara and Arabian deserts, where dust-induced strong surface cooling (down to -32.9 W/m^2) and an equally strong atmospheric heating (up to 33.0 W/m^2) occur [5]. These values are even greater in spring (-39.3 W/m^2 and 39.8 W/m^2 at the surface and in the atmosphere, respectively) and summer (-54.5 W/m^2 and 38.0 W/m^2 at the surface and in the atmosphere, respectively) when dust loads are maximum over these regions [5]. These opposite DA radiative effects in the atmosphere and at the Earth's surface nearly cancel out, resulting in a small cooling or even heating effect at the TOA, over desert areas such as those included in the Mediterranean region. The change in sign of the SW DDRE at the TOA is attributed to the multiple scattering between the absorbing DA and the highly reflective underlying desert surfaces, thus highlighting the important role of surface albedo. On the other hand, the LW DDREs are generally smaller in magnitude and of opposite sign compared to the SW DDREs [6–8] and, for this reason, many studies do not take it into account [9–11]. The magnitude of LW DDREs depends on dust radiative properties [12], but also on several other parameters, such as dust load, coarse/fine mode ratio, dust vertical distribution, and surface temperature and albedo [13]. Albeit smaller than the SW DDREs, the LW DDREs can be significant (reaching up to 26% of the SW DDREs) and counteract the SW cooling effect at the TOA [13].

Apart from their DDRE, DAs play a significant role in the Earth–atmosphere system through their interaction with clouds, since they act as Cloud Condensation Nuclei (CCN) and Ice Nuclei (IN), thus modifying the cloud composition and number of droplets and ice crystals and altering their physical and optical properties. Indeed, as shown by several measurement campaigns [14] and confirmed by laboratory studies [15], dust particles can modify several cloud properties (i.e., liquid water path, cloud fractional coverage) [16] by influencing the particle size distribution, cloud thickness, spatial extent, lifetime, and precipitation [17]. Although near to their sources, DAs contain insoluble materials (such as aluminosilicate clays and carbonates), and field observations have shown that many of the transported dust particles contain nitrates, which are formed during their transport in the troposphere [18,19]. In addition, DAs free of any coatings enhance ice formation through the deposition nucleation mechanism at low supersaturations (10–20%, [20]). On the other hand, for DAs coated with chemically insoluble materials, the nucleation tends to occur at higher supersaturations through the adsorption mechanism [20]. In particular, due to their abundance, mineral DAs act as efficient IN in the atmosphere, ultimately stimulating the formation of cirrus clouds [17]. Specifically, in the eastern Mediterranean, collocated lidar–radar observations have shown a significant presence of mixed-phase clouds formed at the top of dust layers [21]. In general, dusty clouds have higher droplet concentrations and smaller droplet sizes compared to pristine clouds [22]. This increases cloud reflectivity and lifetime while reducing the cloud precipitation efficiency. Such an inhibition of precipitation due to dust was confirmed in the eastern Mediterranean using satellite and aircraft observations [23]. In contrast, an increased concentration of large dust

particles may act as efficient water vapor condensers and drop/crystal accumulators, thus promoting the formation of precipitation [24,25]. Ice latent heat increases the buoyancy and vertical velocities and thus the vertical extent of clouds [26].

From the above, it is clear that DAs are not only a very important climate factor but also a complex and uncertain one. These complications and uncertainties are associated with the simultaneous dust–radiation and dust–cloud interactions, which may have contrasting effects on cloud and precipitation formation (e.g., on the development of mesoscale convective systems in North Africa [27]). The uncertainty of DAs in climate prediction is partly caused by their variable composition and their mixing with other substances in the atmosphere, which results in variable physical and optical properties, as well as by their high spatial and temporal variability. In addition, as described before, DAs interact with clouds through many different processes depending on DA age (e.g., fresh or aged DA) and cloud conditions (e.g., cloud droplet concentrations, relative humidity). In some cases, multiple processes are activated, while different processes compete with each other. Another uncertainty factor of DAs, cited in the last IPCC review [28], is the quantification of the response of dust emission to climate change, since it is sensitive to changes in climate and land use [28].

Although DA emission does occur at high latitudes, such as in Alaska or New Zealand [29,30], it mainly takes place over the world's arid and semi-arid regions [31,32]. Moreover, the smaller dust particles emitted into the atmosphere above desert areas, under favorable atmospheric conditions, rise to upper atmospheric levels, from where they can travel long horizontal distances driven by atmospheric circulation. Characteristic examples of DA transport are those taking place from Asian deserts to northern China and the Pacific Ocean [33,34] and from N. African deserts to the Tropical Atlantic Ocean [33,35–37], Gulf of Guinea [38], and Mediterranean Basin (MB) [39–43]. The MB, due to its proximity to the world's greatest deserts of N. Africa and the Middle East, is frequently affected by dust transport events. This results in the occurrence of so-called [39] Dust Aerosol Episodes (DAEs), which take place at local (pixel-level) scales over the greater MB. When such DAEs have a great spatial extent during a specific day, this day is called a DAED, and when consecutive DAEDs take place, then the so-called dust aerosol episode cases (DAECs) occur, which are spatiotemporally extended/intense dust episodes. The Mediterranean DAEs take place all year round, driven by favorable atmospheric circulation [44], with the maximum frequency of occurrence in spring and summer [39,40]. When such episodes take place, they perturb the regional energy budget [8,45,46], cloud regime [47–49], and atmospheric temperature structure [50]. All these effects, which are very important to the MB weather and climate, deserve to be further studied at the highest possible temporal and spatial resolution using state-of-the-art tools that should be thoroughly evaluated. This is in the aim of the present study, which investigates in detail the DDREs, as well as their effects on the MB temperature structure, cloud regime, and atmospheric dynamics, arising from a specific Dust Aerosol Episode Case (DAEC) that took place from 16 to 18 June 2016 over the central and eastern MB. During this DAEC, mixed-phase clouds, which did not exist a day before (15 June 2016), were formed over the dust export regions [50]. The DA existed in two atmospheric layers, one near the surface, which is more intense near the source areas, and an elevated layer between 2 km and 6 km above sea level. Reduced temperature gradients as well as temperature inversions were also observed below the elevated dust layer. Here, the DDREs are computed with an improved version of the FORTH (Foundation for Research and Technology-Hellas) deterministic spectral Radiation Transfer Model (RTM) [51,52] along with state-of-the-art satellite and reanalysis datasets providing the necessary RTM input data. The estimated SW fluxes are evaluated against reference data, and the computed DDREs are used to interpret the reduced temperature gradients and the formation of temperature inversions during the DAEC found in [50].

Although the DDREs of intense DAECs over the MB have been investigated in previous studies, most of them are spatially limited, since they are based on ground-based measurements [7,53,54]. The aerosol DREs over the entire MB were computed for the

first time by [55] at a monthly and 2.5° latitude–longitude resolution using satellite and reanalysis data as input to the FORTH RTM [51,52]. However, in that study, the calculated DREs refer to the total aerosol effect and not to that of dust alone (DDRE), while they also refer to background aerosol conditions and not to dust episodes. In a step forward in this direction, [8] estimated the DDRE under high-dust-load conditions during 20 Mediterranean DAECs, using the NMMB-MONARCH model. In addition, [45] calculated the DDREs of an episode that took place on February 2015 over the central MB, using the WRF-Chem model. The radiative effect of the same dust episode was also investigated by [56] who conducted a detailed study based on the synergetic use of satellite and ground-based data, as well as model simulations. An important difference of the current study to those by [45,56] is that the studied episode here took place in summer, when the incoming solar radiation at the MB is maximum, thus maximizing the DDREs. Apart from this, the present study tries to address some issues not covered by the previous two studies, for example, providing information about the vertical profiles of DDREs, while it uses a detailed-spectral-resolution RTM, against the broadband RTM or chemical transport models used in the previous studies, and closely follows-up (on a 3-hourly basis) with a longer (3 days against 2 days in previous studies) intense dust episode in the central and eastern MB. Other additional information provided in the present study is the impact of DDREs on atmospheric dynamics, investigated in detail based on several parameters, namely dust-induced heating rates and resulting vertical velocity and buoyancy. In addition, the comparison of the results of the present to those of few previous studies is useful and necessary to reduce the degree of uncertainty of DDREs. This is important given the still-too-large uncertainty in the radiative forcing due to aerosol–radiation interactions (-0.6 to 0.0 W/m^2), which is partly due to the utilized models, even RTMs [57]. The specific version of the FORTH RTM used in the present study allows more safe conclusions to be made because: (i) it runs under all-sky conditions using the latest available version of the International Satellite Cloud Climatology Project (ISCCP) data (ISCCP-H), which provides unique and well-tested cloud optical properties; (ii) it operates at reasonably high spatial ($0.5° \times 0.625°$) and temporal (3-hourly) resolutions, covering the entire area of the MB; (iii) it uses analytical vertical profiles of aerosol (and dust) optical properties, which strongly affect the estimation of DREs for absorbing aerosols, such as dust [46]; and (iv) it yields detailed 3-D distributions of solar fluxes and DDREs. The quality of the estimated DDREs is ensured by the thorough evaluation of RTM fluxes performed against reference fluxes at the surface (from the Baseline Surface Radiation Network (BSRN) stations) and at the top of the atmosphere (from Clouds and the Earth's Radiant Energy System (CERES)).

2. Materials and Methods

2.1. The Determination of the Dust Episode Case

The DAEC of 16 to 18 June 2016, which is studied here, was identified using a satellite algorithm, based on key aerosol optical properties that are a measure of aerosol load, size, and absorptance. Specifically, the algorithm, which is described in detail in [39], uses level-3 daily $1° \times 1°$ gridded spectral Aerosol Optical Depth (AOD) data from the Moderate Resolution Imaging Spectroradiometer (MODIS) Aqua Collection 6.1 and corresponding Aerosol Index (AI) data from the Ozone Monitoring Instrument (OMI) Aura OMAERUV databases. The algorithm, which ran over the broader MB for the study period 2005 to 2019 [39], operates on a daily basis and on a pixel level to first identify the presence of DAs over the specific pixel and on the specific day. The selected study region (broader MB extending from 9.5° W to 39.5° E and from 29.5° N to 47.5° N) is shown in Figure 1, where a smaller region (yellow frame), over which the 16–18 June 2016 dust export took place and regional averaging was applied to DRE values (see Section 3.5), is also displayed. The algorithm operates whenever the following specific criteria are met: (i) the Ångstrom Exponent (a), calculated using the original MODIS spectral AOD information, is less than 0.4 ($\alpha \leq 0.4$), and (ii) the AI is greater or equal to 1 ($AI \geq 1$). In those cases, i.e., when dust dominates in the atmosphere overlying the specific pixel,

another threshold is applied to ensure the occurrence of a strong or an extreme DA Episode (DAE), which is the case whenever AOD_{mean} + 2STDV $\leq$ AOD $\leq$ AOD_{mean} + 4STDV and AOD $\geq$ AOD_{mean} + 4STDV, respectively. Then, if at least 30 pixels undergo strong or extreme DAEs on a specific day, this day is considered to be a DAE Day (DAED). For each identified DAED, the algorithm outputs information about the pixel-level dust loading (AOD) and the number of DAEs. Three such DAEDs, on 16, 17, and 18 of June 2016, were identified by the satellite algorithm, yielding the investigated DAEC in this study. Note that the examined DAEC in this study is one of the 98 DAECs (with duration of n (n $\geq$ 1) sequential DAEDs) consisting of the 166 overall DAEDs identified by the algorithm from 2005 to 2019 [39]. This examined DAEC was selected because: (i) it took place in summer, when the cloud fraction (CF) over the MB, and especially over its southern parts, is low, while the incoming solar radiation is high; (ii) its 3-day duration enables the observation of the evolution of the dust export from North Africa in parallel with the evolution of cloudiness and temperature fields; and (iii) it has extended spatial coverage of the MB, covering 8% of its area. Thus, the selected DAEC, apart from being intense, is also long and spatially extended.

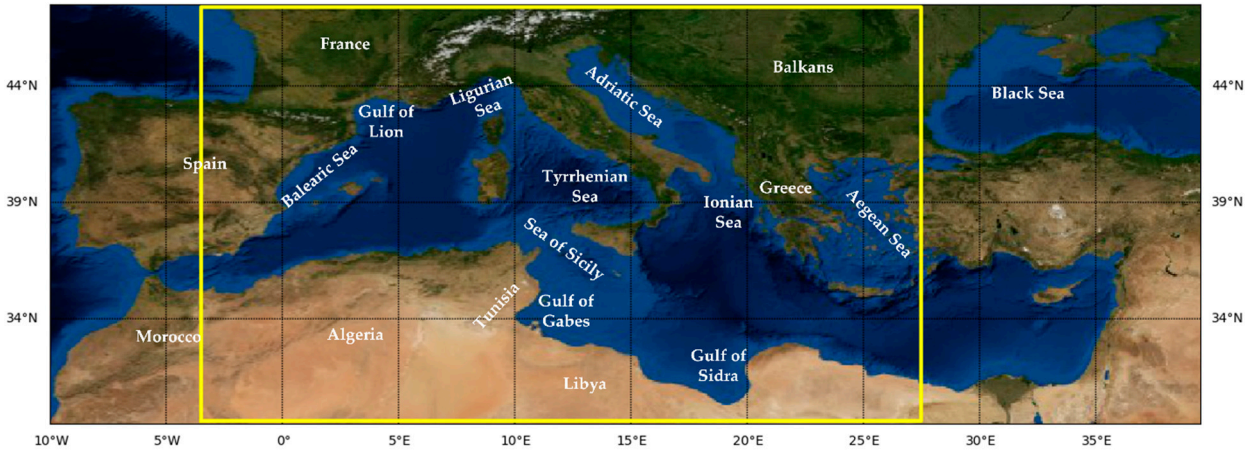

Figure 1. The study region, along with the sub-region (yellow frame) for which 3-hourly spatial mean dust DREs (which are shown in Figure 9) are calculated during the three days of the examined DAEC (16–18 June 2016).

2.2. BSRN, CERES, and AERONET Data

The input and output data of the RTM were evaluated through comparisons against corresponding reference data to ensure their reliability, which also guarantees the quality of the computed solar fluxes. The input MERRA-2 aerosol optical depth data at 550 nm were compared to AOD data from 31 AERONET (AErosol RObotic NETwork [58]) stations located in the broader MB (Figure S1). The AERONET data were interpolated from the available wavelengths of 440 nm and 675 nm, whereas hourly mean values of AERONET measurements were calculated to compare with the corresponding MERRA-2 data. The RTM solar fluxes at the Earth's surface were compared against corresponding fluxes from 7 Baseline Surface Radiation Network (BSRN [59]) stations located within or near the dust export area (Figure S2) and provided measurements for the study period (16–18 June 2016). Since the FORTH SSR fluxes are computed at 3-hourly time steps, the corresponding time intervals were chosen for stations. The RTM fluxes at the top of atmosphere (TOA) were compared to all-sky Clouds and the Earth's Radiant Energy System—synoptic 1° (CERES-SYN1deg-Level 3 [60]) hourly fluxes, choosing the nearest time step in CERES fluxes after the RTM time. Additionally, the original CERES data, which are available at a 1° × 1° latitude and longitude equal-angle resolution, were regridded to 0.5° × 0.625° grids using the first-order conservative remapping scheme [61] along with the operator "remapcon" from the Climate Data Operators (CDOs). It should be noted that this regridding method,

when applied from low to high resolution, preserves the original coarse grid structure and does not affect the comparison.

2.3. MERRA-2 Data

The FORTH RTM input dust optical depth, single scattering albedo, and asymmetry parameter, as well as other surface and atmospheric properties, were taken from the MERRA-2 (Modern-Era Retrospective analysis for Research and Applications, Version 2), which is the latest version of global atmospheric reanalysis for the satellite era produced by NASA's Global Modeling and Assimilation Office (GMAO) [62]. It uses both ground-based and satellite aerosol observations, namely: (i) ocean-only reflectances from the Advanced Very High-Resolution Radiometer (AVHRR) instruments, (ii) reflectances from the Moderate Resolution Imaging Spectroradiometer (MODIS), (iii) AOD from the Multi-angle Imaging SpectroRadiometer (MISR) over the bright desert regions, and (iv) AOD observations from the AErosol RObotic NETwork (AERONET) surface station network, and assimilates them using the Goddard Earth Observing System (EOS) Model, Version 5 (GEOS-5) with its Atmospheric Data Assimilation System (ADAS), version 5.12.4. Data are produced on a $0.500^\circ \times 0.625^\circ$ latitude–longitude grid resolution at 72 atmospheric layers between the surface and 0.01 hPa, for the climatological period from 1980 up to the present, and they are available through the NASA's Goddard Earth Sciences Data and Information Services Center (GES DISC) website (https://disc.gsfc.nasa.gov/, accessed on 1 June 2023).

It should be noted that the vertically and spectrally (at 25 wavelengths between 0.25 and 8.5 μm) resolved optical properties, which are required for the RTM calculations, are not directly available from MERRA-2 database, but they are calculated in this study using vertically resolved (in 72 layers), 3-hourly instantaneous aerosol mixing ratios and spatiotemporally collocated relative humidity data, both taken from the "M2I3NVAER" product, along with look-up-tables providing the extinction and efficiency per aerosol type, size bin, and relative humidity [5,63].

MERRA-2 AOD data have been evaluated against corresponding satellite and ground-based data and have been found to operate well against both of them [64]. However, since AOD is a key determining parameter for aerosol DREs [51,55], an evaluation of AOD data was performed for the first two days of the DAEC (16 and 17 June 2016) over 31 AERONET stations (Figure S1) and the results are shown in Figure S3. In this evaluation, the third day (18 June 2016) is excluded since data were not available. MERRA-2 AOD data correlate well with AERONET retrievals (correlation coefficient R equal to 0.85, Figure S3a), while MERRA-2 slightly (by −0.01 or 6.4%) underestimates AOD compared to AERONET. Moreover, as shown in Figure S3b, MERRA-2 closely follows the daily course of AOD, in terms of averages over the 31 AERONET stations and the corresponding MERRA-2 pixels, with relative percent differences mostly within ±20%. The scatter plot comparison between the SSA of MERRA-2 and AERONET over 8 stations in the MB during the study episode (16–18 June 2016), based on a low number of compared data pairs (N = 33), reveals an underestimation of MERRA-2 SSA (by −0.01 or −1.2%) against AERONET measurements (Figure S4).

2.4. ISCCP-H Data

Cloud properties, namely cloud amount, optical depth, and top pressure, used in the RTM were taken from the ISCCP H-series climate data, which contain level 2 and 3 products for monitoring cloud and surface properties. These data are derived from both geostationary and polar-orbiting satellite imaging radiometers with one visible (VIS ≈ 0.65 ± 0.05–0.20 μm) and one infrared (IR ≈ 10.5 ± 0.5–0.75 μm) "window" channels. There are several improvements of the ISCCP H-series compared to its predecessors C- and D-series, including quality control measures, use of modified ancillary inputs, higher-spatial-resolution input and output products, and calibration refinements [34]. The database, which covers the period from July 1983 to December 2018, and it is planned to extend to the present, constitutes the longest combined geostationary- and polar-orbiter-

satellite-based climatology of cloud properties. All ISSCP-H data products are available on https://doi.org/10.7289/V5QZ281S (accessed on 1 June 2023). Here, the level-3 gridded ISCCP HGG Basic data, available at a 1° equal-angle grid spatial and 3-hourly temporal resolution, were used. The original ISCCP data were regridded at the MERRA-2 spatial resolution (0.500° × 0.625°) using the first-order conservative remapping scheme [61] and the operator "remapcon" from the Climate Data Operators (CDOs).

2.5. The FORTH RTM

The FORTH RTM [51] has evolved from a radiative convective model originally developed by [52]. It has been applied in global [5,51,65,66], regional [55,67,68], and local [53] studies. The FORTH's RTM performance has been extensively evaluated against surface-based and satellite reference radiation fluxes [51,65,69,70], as well as against other SW RTMs [57]. A brief evaluation of the RTM solar fluxes at the Earth's surface and at the TOA against corresponding reference data from 7 stations (Figure S2) of the BSRN ground-based network (left panels of Figure S5) and gridded CERES-SYN1deg satellite measurements over the entire MB and over the 7 BSRN stations (right panels of Figures S5 and S6, respectively), during the three days of the study, the DAEC is provided in Figure S5. The comparison is successful since the 3-hourly matched pairs yielded overall correlation coefficients equal to 0.88 and 0.98, with relative biases equal to 0.8 and 3.5%, respectively, while the RTM TOA fluxes closely follow the intra-daily and the day-to-day variation in the corresponding CERES fluxes.

The FORTH RTM works in the 0.2 to 10.0 μm spectral interval and uses the extraterrestrial solar spectrum of [71] weighted to yield a solar constant equal to 1367 W/m^2. The model solves the monochromatic equation of radiation transfer for a multiple scattering/absorbing atmosphere for 118 individual wavelengths between 0.2 and 1.0 μm and for eight bands between 1.0 and 10.0 μm, following the delta-Eddington method [72]. It accounts for Rayleigh scattering, O_3 absorption in the ultraviolet and visible wavelength areas, and H_2O, CH_4, CO_2, absorptions in the near-infrared, as well as aerosol and cloud scattering and absorption and surface reflection. The FORTH RTM version, which is applied here, ran on a 3-hourly temporal and 0.5° × 0.625° spatial resolution using 3-D aerosol optical properties from MERRA-2 and cloud properties (i.e., cloud amount, optical depth, and top pressure) from ISCCP-H.

The RTM ran one time with all aerosol types and one with all except for DAs and outputted upwelling and downwelling solar fluxes (F_{all} and $F_{no\text{-}DA}$) at the TOA, at the surface, and at 50 levels in the atmosphere. Subsequently, the instantaneous DDREs were calculated from the difference between the fluxes computed by taking and not taking into account DAs, according to:

$$DDRE_i = F_{i,all} - F_{i,no-DA} \quad (1)$$

where i stands for the TOA, surface, and atmosphere (specific atmospheric level). Based on the above-mentioned bias of model fluxes, the expected uncertainty of DDREs should be less than 7%. In addition, the 3-hourly heating rates (K/3 h) caused by the evolving dust episode and subsequent absorption of solar radiation are also estimated in order to yield the effect of the dust DREs on the thermal structure and the dynamics of the Mediterranean atmosphere. The computation is made according to:

$$\frac{\partial T}{\partial t} = \frac{g}{c_p}\frac{\Delta F}{\Delta P}, \quad (2)$$

where $\partial T/\partial t$ is the heating rate, g is the gravitational acceleration, c_p is the specific heat capacity of air at constant pressure (1006 J/KgK), ΔF is the $DDRE_{atm}$, and P is the atmospheric pressure.

Lastly, the buoyancy (vertical acceleration) induced by the DDRE was also calculated using the following equation (derived from Newton's first law and from the ideal gas law):

$$\alpha = \frac{(T' - T)}{T} \cdot g \quad (3)$$

where α is the caused acceleration in m/s^2; T' and T are the atmospheric temperature with and without the DDRE, respectively; and g is the gravitational acceleration.

3. Results and Discussion

3.1. Aerosols, Clouds, and Solar Fluxes during the Evolution of DAEC

To have an easy view of the simultaneous evolution of cloudiness and aerosol loadings over the MB and its areas undergoing the African dust export, Figure 2 displays the geographical distributions of MERRA-2 DOD (left column) and ISCCP-H cloud amount (right column) during the three days of the examined DAEC, i.e., from 16 to 18 June 2016 (values are at 12:00 UTC). The dust export originates from Algeria and Tunisia and extends over the Gulf of Gabes, the Tyrrhenian Sea, Italy, and up to the Adriatic Sea on the first day (16 June 2016, Figure 2i-a) of the episode. Maximum dust loadings (DOD values up to 1.4, reddish colors) are noted on this day over the eastern Tunisian coasts and southern Tunisia inland. During the next two days (17 and 18 June 2016, Figure 2i-b,c) dust export moves eastward, with medium-to-high dust loadings (DOD around 0.5) covering the entire area of Greece and the Balkans. On these days, the maximum DOD values are reduced (reddish colors disappear and maximum DOD values reach up to about 1), compared to the first day of the DAEC, but high loadings cover wider areas of central and eastern MB. As shown in the right column of Figure 2, significant CFs (up to 0.9–1.0) are observed across the dust export path during the three days of the DAEC, against clear-sky conditions or low cloud cover over these areas before (on 15 June 2016) the dust episode, which provides evidence that the evolving Mediterranean dust episode plays a key role in the formation of both liquid- and ice-phase clouds by providing CCN and IN (Figure S7). This was also found by [50], where MODIS CF data were used, instead of those of ISCCP-H. In addition, as shown in this study (Figure 2) and by [50], the clouds over the areas that continued to undergo dust transport on the second and third day of the DAEC (17 and 18 June) either dissipate or diminish, with their cloud top height and temperature decreasing and increasing, respectively (Figure S8). The comparison between the ISCCP-H-based cloud cover of our Figure 2 and the corresponding ones of MODIS (Figure 5 in [50]) reveals that the two cloud products have similar geographical patterns, but ISCCP-H generally overestimates cloud amount, especially over N. Africa and the Aegean Sea. Such an overestimation was also found in [73] who compared the ISCCP-H total cloud amount to that from the Cloud, Albedo, and Surface Radiation dataset from AVHRR data-edition 2 (CLARA-A2) surface-based observations at 22 meteorological stations in Europe, from the European Climate Assessment & Dataset (ECA & D). This overestimation may be associated with the viewing angle of the geostationary satellites or to the detection of cirrus clouds by satellites, which is not possible for surface observations. Additionally, a comparison between CFs from previous versions of ISCCP and MODIS datasets over Europe made by [60] revealed an overestimation of ISCCP in spring and summer.

The DDREs are strongly dependent on three key aerosol (dust) optical properties, namely optical depth, single scattering albedo (SSA), and asymmetry parameter (AP), with DOD and SSA being the primary ones [55]. The geographical distribution of MERRA-2 SSA and AP at 550 nm during the three days of the examined DAEC, as well as one day before and after the DAEC, is shown in Figure S9 (DOD is shown in Figure 2 and has already been discussed). The SSA values over the dust export regions, during the three days of the DAEC, vary between 0.92 and 0.94, i.e., values that are representative of Saharan DAs [74]. Similar and slightly lower (0.91–0.92) SSA values are observed over N. Africa. Higher SSA values, up to 0.95 (yellowish colors) or 0.97 (reddish colors), are observed over Mediterranean Sea areas not undergoing dust export and dominated by non-absorbing sea-salt aerosols. Even higher SSA values (larger than 0.98, deep red colors) exist over the Atlantic Ocean, where dust and other continental aerosols are absent, in contrast to

the closed Mediterranean Sea surrounded by European and African land areas. Regarding the geographical distribution of MERRA-2 AP, it varies between 0.74 and 0.76 over both N. Africa and dust export regions (Figure S9), indicating the dominance of DA [74]. In general, larger AP values occur over areas with coarse maritime and dust aerosol loadings.

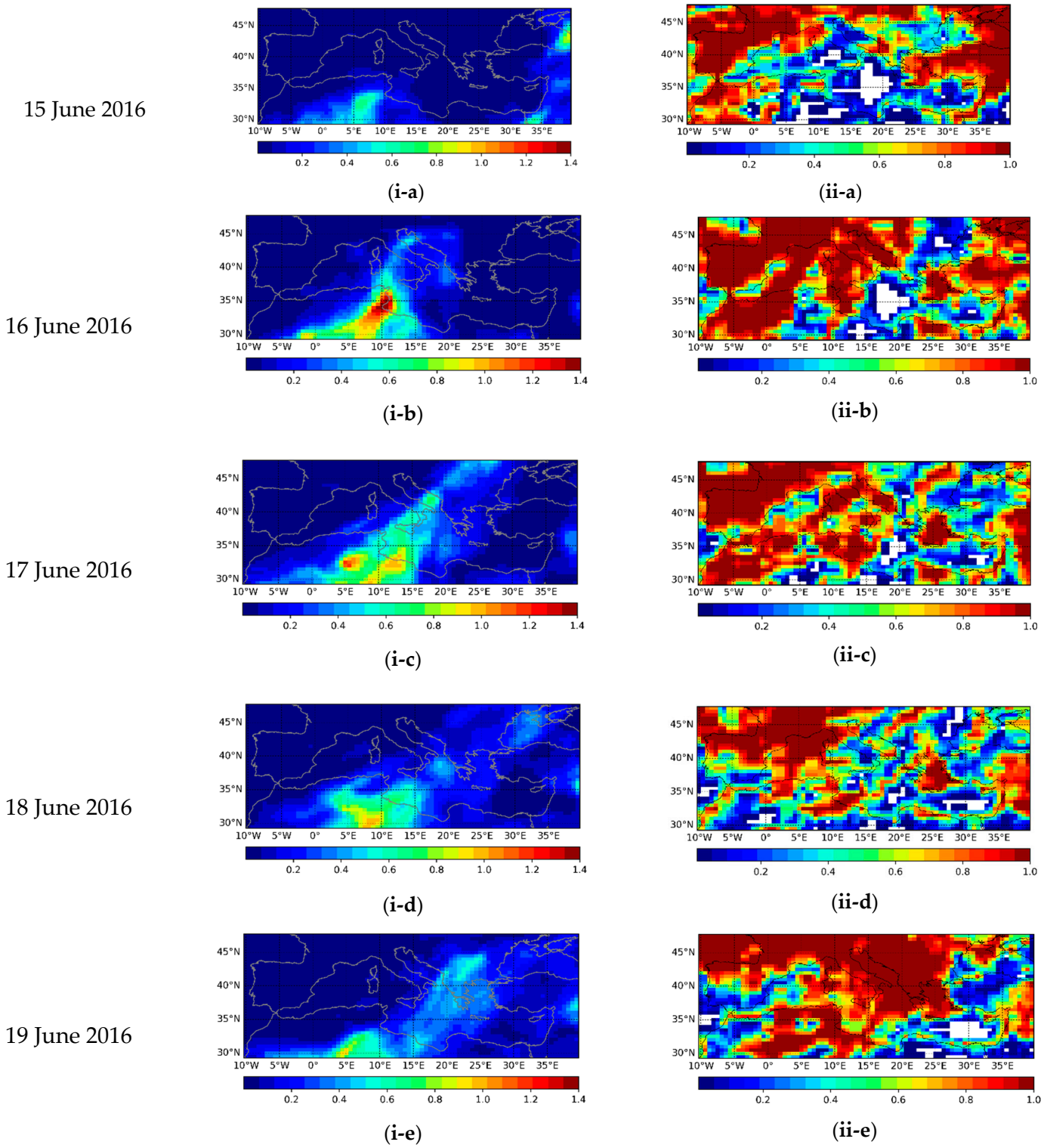

Figure 2. Geographical distribution of MERRA-2 DOD (left column, (**i**)) and ISCCP-H cloud amount (right column, (**ii**)) during the day before (first row, (**a**)), the first (second row, (**b**)), second (third row, (**c**)), third (fourth row, (**d**)), and the day after (fifth row, (**e**)) the DAEC that took place during 16–18 June 2016 over the Mediterranean Basin. Results are given at 12:00 UTC of each day.

Apart from the aerosol optical properties, the DDREs are strongly dependent on the available solar radiation fluxes [55]. These fields, namely the absorbed solar radiation at the TOA, in the atmosphere, and at the surface of the broader MB, including the African dust export areas, are given in Figure 3. The solar radiation fluxes are computed for all-sky conditions, i.e., including the presence of clouds, during the three days of the DAEC and are given at 12:00 UTC of each day. At the TOA, the absorbed solar radiation fluxes (Figure 3, first column) are strongly influenced by clouds (Figure 2, second column) and secondarily by other parameters such as aerosols and surface albedo. On the first DAEC day, the absorbed solar fluxes at the TOA vary from 450 to 1150 W/m^2, with lower values over areas covered by clouds, such as the northwestern Algerian coasts, and over the areas along the axis extending northeasterly, passing over the Balearic Sea and reaching up southeastern France and the Alps, as well as the areas along a second axis of cloud-covered areas extending northeasterly from the Tunisian coasts over the Tyrrhenian Sea, central Italy, and up to the northern Adriatic Sea (see Figure 2). Nevertheless, not all similarly cloud-covered areas absorb the same solar radiation. For example, clouds along the second axis, in the central MB, absorb significantly less SW radiation than clouds along the first axis, in the western MB, by as much as 100–200 W/m^2, though having similar cloud fractions (larger than 0.8–0.9, Figure 2ii-a). These differences are attributed to the different cloud optical thickness (COT) of these two cloudy areas, being about 6 to 24 in the western and less than 5 in the central MB (Figure S8), highlighting the primary role of COT in the perturbation of solar radiation [65,75]. In contrast, the highest absorbed solar fluxes at the TOA (larger than 1000 W/m^2) are observed over the cloud-free Mediterranean Sea areas, which also have low surface albedo. The role of surface albedo is evidenced by the significant differences (of about 200 W/m^2) between the TOA-absorbed SW values over the low-surface-albedo central and eastern Mediterranean Sea (deep reddish colors) and the more reflective adjacent continental coastal areas of North Africa (Libya and Egypt, greenish and yellowish areas). Similar findings, underlying the primary role of clouds and surface albedo for the absorbed solar flux at the TOA, are found for the second and third days of the DAEC (Figure 3i-b and Figure 3i-c, respectively).

The geographical patterns of the atmospheric absorbed solar radiation (second column in Figure 3) are governed by clouds and aerosols as well as the available solar radiation. Most aerosols, except for strongly scattering ones such as sulfate and sea-salt, increase the SW atmospheric absorption. On the other hand, clouds strongly scatter the SW radiation, while modifying (increasing or decreasing) the absorbed solar radiation in the atmosphere through different mechanisms. For example, due to their high albedo, clouds increase the upward SW flux and thus the SW absorption by ozone and water vapor, or absorbing aerosols (e.g., dust or biomass burning) above them [76]. The SW absorption is also increased within the cloud layers, because they absorb more near-infrared (NIR) solar radiation than water vapor does [77]. On the contrary, clouds can reduce the SW atmospheric absorption by shielding the water vapor and consequently the solar absorption below them. The first two mechanisms dominate the third one in high clouds; in middle clouds, the three mechanisms nearly cancel out; while the third mechanism predominates in low clouds [75]. On the first day of the DAEC (16 June 2016, Figure 3ii-a), there is a clear contrast between the western and eastern MB, where aerosols and clouds practically do not exist (Figures 3 and S8). The largest SW atmospheric absorption (400–450 W/m^2) is observed over northeast Algeria, Tunisia, and Tunisian coasts, where DOD is also maximum (Figure 2). Secondarily high absorption is observed over an area along a northeasterly oriented axis, extending from the boundaries between Morocco and Algeria up to the northernmost part of the western Mediterranean Sea, where high-level clouds exist (Figure S8). The patterns of atmospheric solar absorption and their explanation are similar for the next two days of the DAEC, namely on 17 and 18 June 2016. As it concerns the patterns of absorbed solar radiation at the MB's surface (right column of Figure 3), during the whole DAEC, they have many similarities with the patterns of absorbed radiation at the TOA, and contrasts with the patterns of absorbed radiation in the atmosphere, showing

that surface absorption accounts for the largest part of the overall planetary (TOA) SW absorption over the study region. A strong solar absorption, with values from 400 up to 1000 W/m^2, occurs over the largest part of the MB during the three days of the DAEC. The largest values (reddish colors) appear over areas with no or few clouds and aerosol loads, e.g., the eastern Mediterranean Sea, whereas the smallest surface solar absorption (down to 150–200 W/m^2, bluish colors) is observed where clouds or aerosols exist and drastically reduce, through scattering and absorption, the solar radiation reaching the surface [5,75].

3.2. Geographical Distribution of DDREs

The geographical distribution of the instantaneous (12:00 UTC) all-sky DDREs (at TOA, in the atmosphere, and at the surface), during the three days of the examined DAEC, are illustrated in Figure 4. The corresponding daily mean all-sky DDREs are shown in Figure S10. The spatial patterns of DDREs in the atmosphere (middle column of Figures 4 and S10) and at the region's surface (right column of Figures 4 and S10) are quite similar to those of the geographical distributions mainly of DOD (Figure 2i) as well as dust SSA (Figure S9), underlining the determinant role of DA loads for the perturbation of the solar radiation budget. Dust particles increase the absorption of solar radiation everywhere (positive values of DDREs in the maps of Figure 4ii), by as much as 187 W/m^2 at 12:00 UTC and 70 W/m^2 on a daily mean basis (Figure 4ii and Figure S10i), over areas with maximum DOD values (Figure 2i). This absorption leads to an atmospheric radiative heating effect, as discussed later (Section 3.5). Larger atmospheric DDREs are observed during the first day of the DAEC (values up to 168 W/m^2, Figure 4ii-a and Figure S10ii-a), when DOD is also largest (Figure 2i-a), than in the next two days (values up to 138 W/m^2). This day-to-day decrease in the magnitude of atmospheric DDREs is due to the transport of dust from the source African areas to the MB and the consequent spreading out of their loads to areas as far as the northern Balkan peninsula and the Black Sea (Figure 2). At the surface, very similar geographical patterns, but with a negative sign and even greater magnitude, are observed over the entire MB (right column of Figures 4 and S10). The greater magnitude of the surface DDREs is attributed to the scattering of dust, which cuts off the downward solar radiation, as well as to dust absorption. The decreased surface solar radiation, caused by dust, produces a solar dimming and a subsequent SW radiative cooling. The surface DDREs take values between zero, over areas with zero or very low DOD, and down to −200 W/m^2 at 12:00 UTC (−60 W/m^2 on a daily basis) over dust export areas, e.g., over Tunisia's eastern coasts on the first day of the DAEC (16 June 2016, Figure 4iii-a, deep blue colors). Again, as also found for the atmospheric DDREs, the surface DDREs gradually decrease from the first to the second and third days of the DAEC (largest values equal to −144 and −113 W/m^2, respectively). In another study [45] using WRF-Chem for estimating the net (SW + LW) clear-sky DDRE of a dust episode that took place on February 2015 over the MB, the researchers found an atmospheric radiative heating up to +147 W/m^2 and a surface radiative cooling as strong as −252 W/m^2. The slightly different (mainly larger) values compared to those in the present study are mainly attributed to the cloud-free conditions considered in [45] as well as to differences in dust loads (up to 4.5 in [45] against 1.4 in the present study) and the used models (WRF-Chem against FORTH-RTM). Similar or even larger atmospheric and surface DDREs than those of the present study have been estimated by [8] with the NMMB-MONARCH model during 20 intense and widespread dust outbreaks, which affected the broader MB from 2000 to 2013. In addition, in [56], based on the chemical transport model (CTP) and RTM simulations, a reduction in the Global Horizontal Irradiance (GHI) as large as −200 W/m^2 due to the presence of a dust plume that affected the MB on 1st February 2015 was found. Apart from studies with large (regional) spatial coverage, there are also some local studies of DDREs. Thus, the DDRE during a dust intrusion on July 2002 at Lampedusa Island was estimated by [46], reporting lower values at the surface (maximum perturbation of 33 W/m^2 against 75 W/m^2 in this study). This difference is attributed to the lower AOD (up to 0.2) in [46] than in the present study (up to 1.4). Yet, surface and atmospheric DREs as large as −215 and 139 W/m^2,

respectively, similar to ours, have been estimated in [53] using a similar version of the FORTH RTM, used in this study, at Crete island in the eastern Mediterranean. At the TOA, both positive (planetary warming, reddish colors) and negative (planetary cooling, bluish colors) DDREs are observed (left column of Figure 4). Specifically, negative values (as large as -40 W/m^2) are noted over the Mediterranean Sea and most of the European and North African land areas, while positive values (up to 70 W/m^2) occur over areas mainly of N. Africa, which are covered by high dust loadings (see left column of Figure 2). The sign change of the dust DRE at the TOA is attributed to the presence of absorbing dust aerosols overlying high-surface-albedo desert areas [51,55,65,78].

In Figure S11, the geographical distributions of the percent relative perturbation of the regional SW radiation budget, namely of the absorbed solar radiation at the TOA, in the atmosphere and at the surface, by dust aerosols during the DAEC are presented (Figure S11a–c). Significant modifications of the SW fluxes are observed, reaching 35% (decrease) and 45% (increase) at the MB's surface and in the atmosphere, respectively, especially over areas overloaded with the heaviest dust loadings (DODs). The radiative perturbations at the surface (cooling) and in the atmosphere (warming) are counterbalanced, leading to smaller perturbations (up to about 5%, either cooling or warming) at the TOA. The geographical features of the relative percent DDREs (Figure S11), including the gradual reduction in the tilt of the axis along which the dust export takes place over the MB, and its slow eastward shift, are identical to those of the corresponding absolute DDREs (Figure 4). The existence of maximum values, in both distributions, over areas with the largest dust loadings proves again that the dust optical properties, and in particular the optical depth, are the major drivers for DDREs.

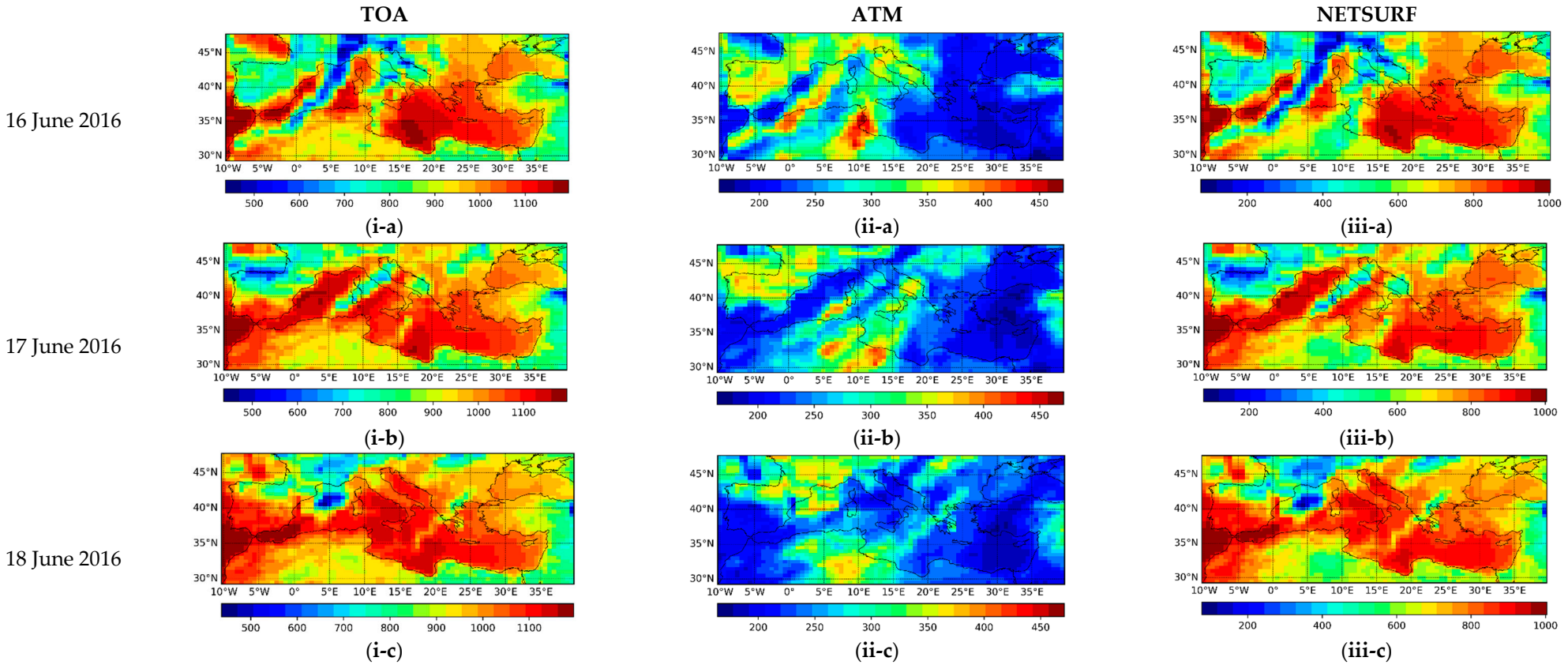

Figure 3. Geographical distribution of: the absorbed solar radiation (in W/m^2) at the top of the atmosphere (left column, (**i**)), in the atmosphere (middle column, (**ii**)) and at the Earth's surface (right column, (**iii**)) for the first (first row, (**a**)), second (second row, (**b**)), and third (third row, (**c**)) day (at 12:00 UTC) of the dust episode that took place during 16–18 June 2016 over the Mediterranean Basin.

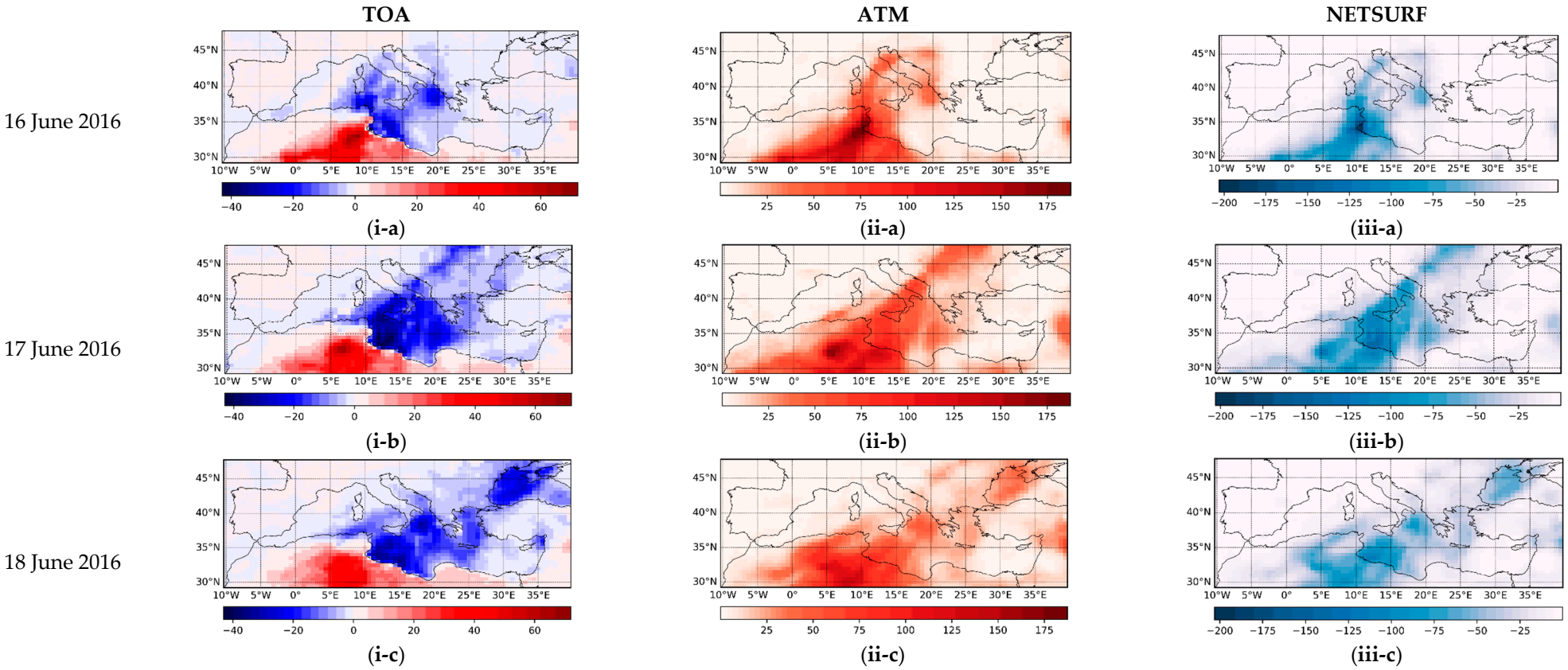

Figure 4. Geographical distribution of the dust direct radiative effect (in W/m^2) on the absorbed solar radiation: at the top of the atmosphere (left column, (**i**)), in the atmosphere (middle column, (**ii**)), and at the Earth's surface (right column, (**iii**)) for the first (first row, (**a**)), second (second row, (**b**)), and third (third row, (**c**)) day (at 12:00 UTC) of the dust episode that took place during 16–18 June 2016 over the Mediterranean Basin.

3.3. Vertical Profiles of DA Effects on SW Radiation, Thermal Structure, and Atmospheric Dynamics

Vertical variations in the sign and magnitude of DDREs, but also of aerosol DREs in general, are expected during intense dust transport events, such as the examined DAEC here, due to modifications either of the transferred solar radiative fluxes or of the aerosol optical properties. The absorption and scattering of DAs are not vertically homogeneous, but depends on the vertical distribution of DAs as well as on the available solar radiation, leading, for example, to stronger dust-induced atmospheric heating effects at altitudes where the DA load is high [66]. Moreover, the vertical position of aerosols relative to clouds is also important, changing the sign of the TOA DDRE [79,80], while the vertical distribution of aerosols alters both the aerosol–radiation and aerosol–cloud interactions, possibly enhancing the atmospheric warming [71]. In addition, the vertically resolved aerosol's (dust included) radiative effects also depend on the vertical distribution of water vapor with respect to the aerosol layers [81], causing further complexity. Finally, DAs also produce considerable effects on LW radiation, producing vertically variable atmospheric cooling and surface warming [82]. These inhomogeneous and vertically variable DA radiative heating and cooling effects, in conjunction with the warm advection, which takes place during the transport of DAs from the hot desert areas of N. Africa to the MB, modify the region's atmospheric temperature structure and stability. Such modifications due to DAs, such as the increased atmospheric stability affecting the downward mixing of energy and cloud formation [4], have been investigated over the Tropical Atlantic Ocean [37], Australia [83], and Asia [84], leading to the conclusion that DAs cause temperature inversions and/or decreased temperature gradients in the lower atmospheric layers (i.e., from 1 to 3 km above the ground). Concerning the Mediterranean Basin, the first study dealing with the modification of temperature lapse rates due to the presence of high dust loads was made by [50], who selected the same DAEC with the one investigated in the present study (16–18 June 2016). Performing a study based on observational satellite and reanalysis data, they investigated for the first time the modification of temperature structure and lapse rates over the MB in the presence of high dust loads. They found that the transport of African DAs takes place in two atmospheric layers, one near the surface, which is more intense near the source areas of N. Africa, and an elevated second layer between 2 and 8 km, resulting in systematic intense temperature inversions (as strong as 20 K/km) and/or reduced temperature lapse rates just below the elevated dust layer. The aim of the present section is to interpret these findings based on the SW atmospheric DDRE and to estimate its contribution to the overall observed atmospheric heating, lapse rates, and temperature inversions, taking into account that all these are formed under the action of other processes than the transfer of SW radiation and induced SW DDREs, namely the dust LW radiative effects, the horizontal and vertical transfer of sensible and latent heat fluxes, the thermal conduction, as well as the adiabatic heating/cooling associated with convective air motions.

In Figures 5–7, specific vertical cross-sections of the dust extinction coefficient ($\sigma_{ext,dust}$, in km^{-1}), solar atmospheric DDRE (in W/m^2), atmospheric heating rates (HR, K/3 h), and temperature gradients (γ, in K/km) across the pathway of the exported dust during the three days of the DAEC, at 12:00 UTC of each day, are shown. The slant path of the first day of the DAEC (16 June 2016, Figure 5e) extending from Morocco, passing through the central Mediterranean Sea and Italy, and reaching up to the NE Balkans, is selected to cover areas affected or not by the African dust export, in order to highlight the effect of DAs. Indeed, a distinct dust layer extending from 37° N–5° E to 45° N–20° E (Figure 5a,e), namely from the Algerian coasts to the northwestern coasts of the Balkans, with $\sigma_{ext,dust}$ values up to 9.1×10^{-2} km^{-1}, is found at altitudes ranging up to about 4–5 km, while reaching the surface over areas between 38° and 41° N. The significant dust loadings in this layer produce, through absorption of solar radiation, a considerable radiative heating (Figure 5b) reaching values up to 4 W/m^2 at heights (up to about 7–8 km) and locations with high dust loadings, namely over areas extending from the coasts of Algeria (37° N–5° E) to Romania (45° N–22° E). It should be noted that the maximum DA SW radiative heating is not observed exactly where the maximum dust loadings occur, but slightly higher in

the atmosphere. This is evident in the aforementioned plot areas between 37° N–5° E and 45° N–20° E, for which the maximum dust loadings extend from the surface up to about 5 km, whereas the maximum SW heating is found between about 3 and 6 km. The different height of maximum dust SW heating and loadings is explained by the fact that the SW atmospheric DDRE is not only dependent on the dust loadings, but also on the available solar radiation, which is decreasing downward. As a direct consequence of the induced solar radiative heating, DAs induce atmospheric heating rates, up to 0.04 K/3 h within the dust layer (Figure 5c). However, it should be noted that the heating rates illustrated in Figure 5, as well as in Figures 6 and 7, refer to atmospheric layers with inhomogeneous depth, ΔP, which increase with height (see Equation (2)). The atmospheric warming caused by the absorption of solar radiation by DAs, where they occur, decreases the magnitude of normal (negative) atmospheric lapse rates. At very few locations, characterized by very small lapse rates, this can lead to temperature inversions. Such reduced temperature lapse rates (down to −0.5 K/km) and intense temperature inversions (up to +9 K/km) are noted just below the elevated dust layer (white and red shaded areas in Figure 5d). The magnitude of the dust-induced atmospheric heating rates seems to be small compared to the magnitude of the prevailing atmospheric lapse rates, which shows that the interaction (absorption) of solar radiation with (by) dust is not the main driver for the formation of the atmospheric lapse rate during the DAEC, which may be driven by other mechanisms, such as the advection of heat or thermodynamic processes. This deserves to be further investigated using tools, such as the WRF-Chem model, accounting for all these mechanisms, and this is planned for a future study. A somewhat larger dust radiative heating, varying from −0.7 to +1.2 K at 12:00 UTC and from −2 to +2 K at 00:00 UTC, was reported in [45] where the WRF-Chem model was used to estimate the effect of a dust episode on the atmospheric temperature (from the difference between model output temperatures accounting and not accounting for DAs), but under clear-skies, which maximizes the heating rates produced by DAs.

On the second day of the DAEC, the selected slant path extends from SE Tunisia to southern Italy (Sicily and Taranto), the Adriatic Sea, and NW Balkans (Figure 6e). Significant dust loadings, larger than those in the first day of the DAEC, occur over the continental N. African areas along the slant path, and off the Gulf of Gabes, from the surface up to 7 km, with maximum loadings ($\sigma_{ext,dust}$ up to 3.6×10^{-1} km^{-1}) within the first two kilometers above the Libyan coasts (Figure 6a). Far from the source areas (i.e., over Italy and the Adriatic Sea), slightly smaller maximum loads ($\sigma_{ext,dust}$ up to 2.0×10^{-1} km^{-1}) are observed within an elevated dust layer near 5 km ASL. On this second day of the DAEC, the SW DDREs are much higher than those on the previous day, becoming maximum (13 W/m^2) within the elevated dust layers (around 5 km ASL, Figure 6b), while they are smaller (2 to 6 W/m^2) at lower altitudes along the rest of the cross-section. Above 5 km, the DDREs take very small (almost zero) positive or even negative (at 9 km ASL, from 31.0° N–10.5° E to 33.0° N–20.0° E) values. The features of the vertically resolved SW heating rates due to DAs (Figure 6c) are identical to those of the corresponding SW DDRE, reaching values up to 0.14 K/3 h around 5 km ASL and down to −0.001 (atmospheric cooling) around 9 km ASL. As it is shown in Figure 6d, an intense (up to +22 K/km) and spatially extended temperature inversion takes place below and within the surface dust layer, namely off the Tunisian and Libyan coasts (32.5° N, 11.5° E) up to the Sicily coasts (36.5° N, 14.5° E). Weaker temperature inversions (up to +6 K/km) and reduced temperature gradients (down to −0.5 K/km) are noted across the rest of the cross-section just below the elevated dust layer (Figure 6d). Again, as already discussed for the first DAEC day, the maximum SW DDREs and heating rates are not found where the maximum DODs exist, namely near the surface above the dust African source areas, but at higher altitudes. This is attributed to the available solar radiation, which gradually decreases with its downward propagation, through the absorbing/scattering dust layer up to about 5 km, but also to the scattering/absorption by other factors such as clouds. Indeed, middle and

high clouds (Figure S8i-b), which exist along the slant path of this day (Figure 6e), further reduce the downward SW solar radiation.

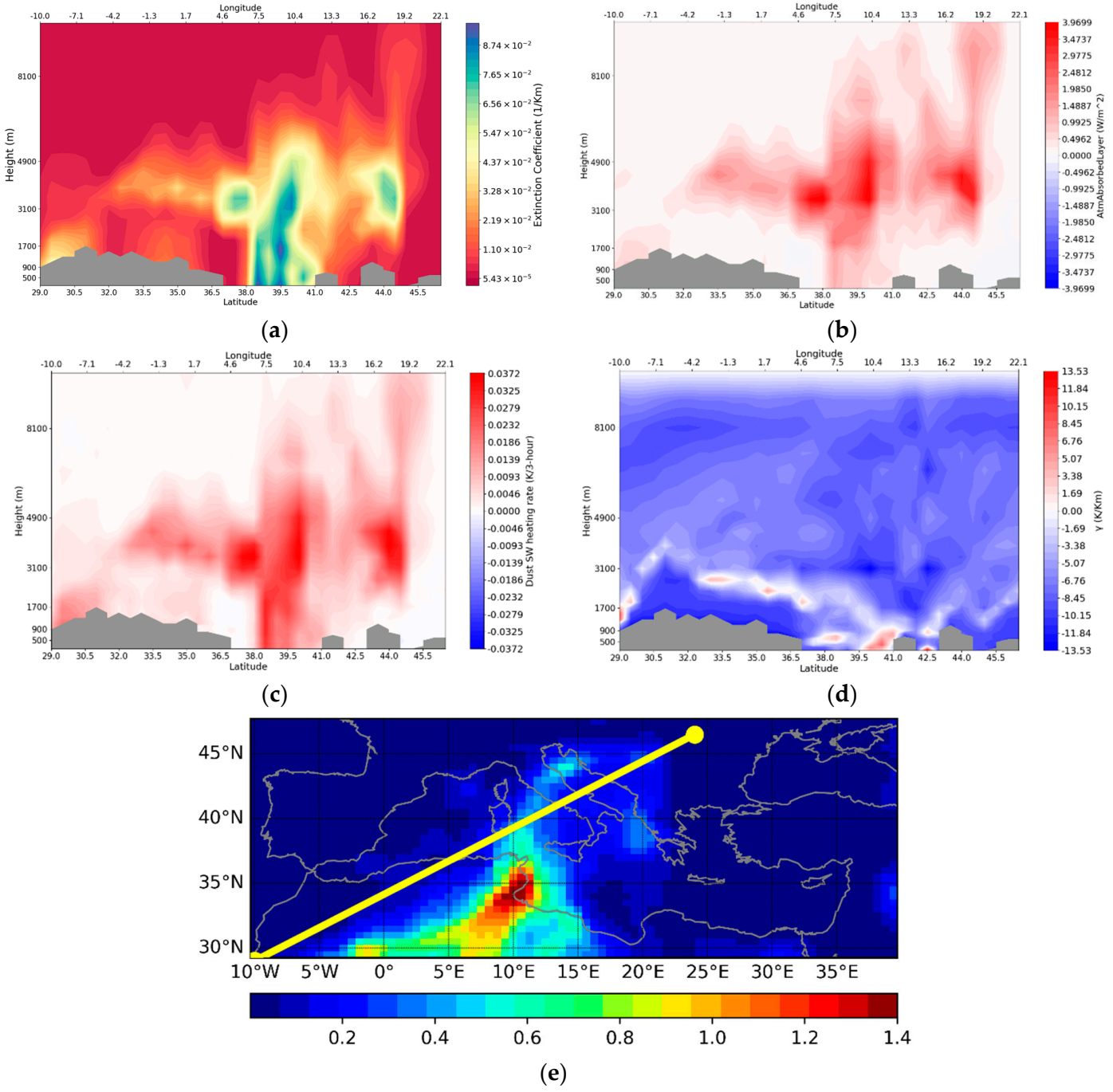

Figure 5. Vertical cross-sections of MERRA-2 dust extinction coefficients (in km^{-1}, (**a**)), dust solar direct radiative effect in the atmosphere (in W/m^2, (**b**)), dust solar radiative heating rates (in K/3 h, (**c**)), and atmospheric temperature gradients (in K/Km, (**d**)), along the slant path across the African dust export into the Mediterranean Basin (shown on the map of DOD, (**e**)), during the first day (16 June 2016) of the dust episode that took place during 16–18 June 2016 over the Mediterranean Basin.

Finally, on the last day of the DAEC (18 June 2016), the selected slant path runs across the dust export axis, which slightly shifts eastward and covers the Ionian basin and the Aegean Sea (Figure 7e). The dust loadings remain high in this third day of the DAEC, with $\sigma_{ext,dust}$ values (yellowish and greenish colors) as large as 1.5×10^{-1} km^{-1} over the

Libyan dust sources and off the Libyan coasts (from 29.5° N–11.5° E to 34.0° N–15.0° E), extending from the surface up to 5 km ASL. A distinct elevated dust layer between 3 and 5 km ASL (bluish colors in Figure 7a) is observed over the Ionian basin and Sea (from 34.0° N–15.0° E to 40.0° N–20.0° E), while a weaker ($\sigma_{ext,dust}$ up to 4.0 × 10^{-2} km^{-1}) elevated dust layer is also observed at similar altitudes over the Balkans (bright orange colors in Figure 7a). Again, as in the previous two days, significant SW DDREs (up to 8 W/m^2, Figure 7b) and heating rates (up to 0.07 K/3 h, Figure 7c) are observed near the dust layer, with the DDREs located a bit higher for the same reasons reported in the previous paragraph, i.e., available solar radiation and significant heating rates down to the surface. The dust-induced absorption of solar radiation, and the consequent radiative heating, decrease again the magnitude of lapse rates in the atmospheric layers overloaded by dust, contributing to the formation of intense temperature inversions (up to +13 K/km) observed below the elevated dust layer and over the colder sea surfaces extending from the Libyan coasts to the Ionian Sea (reddish colors in Figure 7d). Decreased temperature gradients are found along the rest of the slant path and below the elevated dust layer (light blue/white colors in Figure 7d).

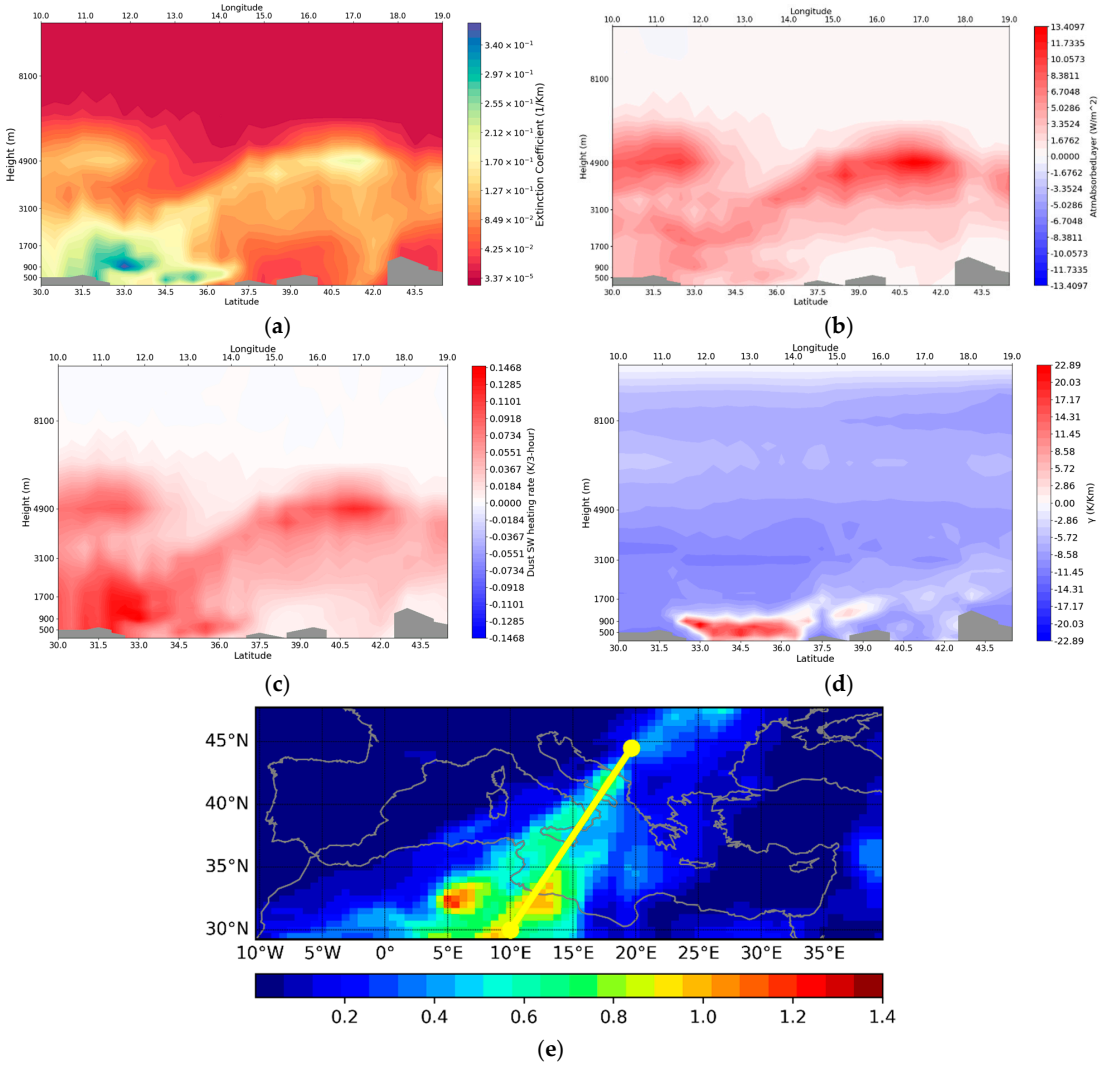

Figure 6. Vertical cross-sections of MERRA-2 dust extinction coefficients (in km^{-1}, (**a**)), dust solar direct ra-diative effect in the atmosphere (in W/m^2, (**b**)), dust solar radiative heating rates (in K/3 h, (**c**)), and atmospheric temperature gradients (in K/Km, (**d**)), along the slant path across the African dust export into the Mediterranean Basin (shown on the map of DOD, (**e**)), during the second day (17 June 2016) of the dust episode that took place during 16–18 June 2016 over the Mediterranean Basin.

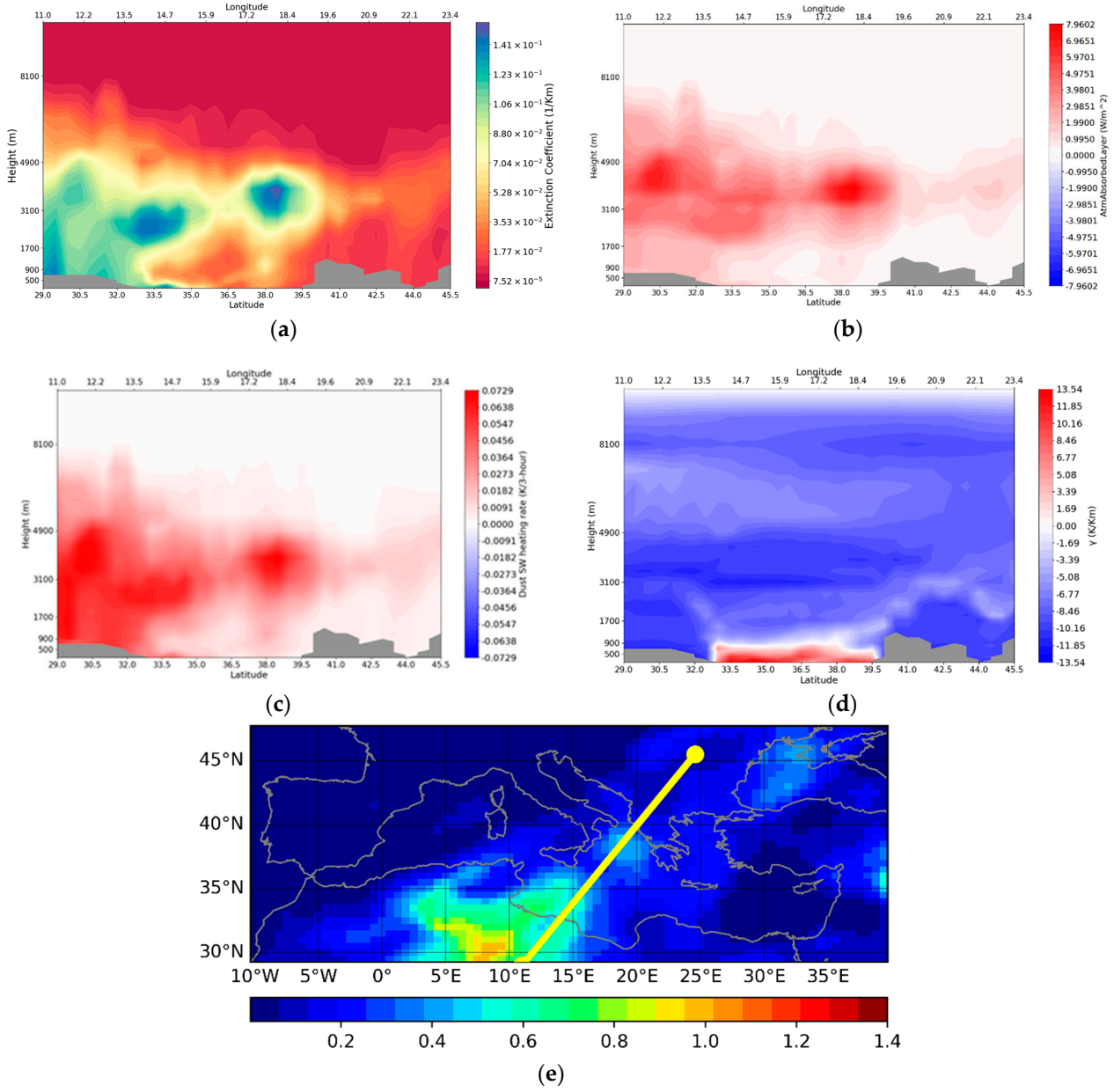

Figure 7. Vertical cross-sections of MERRA-2 dust extinction coefficients (in km^{-1}, (**a**)), dust solar direct ra-diative effect in the atmosphere (in W/m^2, (**b**)), dust solar radiative heating rates (in K/3 h, (**c**)), and atmospheric temperature gradients (in K/Km, (**d**)), along the slant path across the African dust export into the Mediterranean Basin (shown on the map of DOD, (**e**)), during the third day (18 June 2016) of the dust episode that took place during 16–18 June 2016 over the Mediterranean Basin.

3.4. The effect of DA on Buoyancy

The DA-induced heating rates were used to calculate (Equation (3)) the buoyancy (vertical acceleration, α) caused by the SW DDRE. The results, namely the cross-sections of computed DA buoyancy, along the selected slant paths during the three days of the examined DAEC (Figures 5e, 6e, and 7e) are shown in Figure 8 (left column). It is found that during the dust episode, the absorption of SW radiation and the consequent radiative heating induce an upward vertical acceleration of air masses, which is directly proportional to the SW heating rates (Figures 5c, 6c and 7c). The strongest buoyance, i.e., largest values of α (deep red colors), is found close to heights with the highest dust loadings, reaching

0.01 m/s^2 at altitudes up to 5–6 km on the second day (17 June 2016, Figure 8i-b), where/when maximum DDREs and heating rates also occur.

The importance of the induced vertical acceleration of air parcels by DDREs can be appreciated by comparing their values with the corresponding ones of the prevailing vertical velocities of the air (vertical wind V, right column of Figure 8). Although the magnitude of the DA buoyancy appears to be smaller than the magnitude of V by two to three orders of magnitude, it is not insignificant. Thus, for example, on the first day of the DAEC, the vertical wind speed overall varies from −25 m/s (downward motions) to 21 m/s (upward motions, Figure 8i-a). On this day, the vertical velocity and the DA-induced acceleration in the elevated dust layer are 9 m/s and 0.002 m/s^2, respectively. This means that should the DA-induced acceleration persist for 1 min, it would increase the vertical velocity by 0.12 m/s or 1.3%, while should it prevail for 10 min, it would result in a vertical wind speed equal to 1.2 m/s, i.e., it would increase it by 33%.

Dust aerosols either enhance or suppress the convective motions over altitudes having the same (both reddish or bluish) or opposite (reddish-bluish or bluish-reddish) colors. For instance, on the first day of the DAEC, at altitudes up to 1.5 km over 40° N–9.5° E, where negative vertical velocity prevails, the dust-induced buoyancy (positive acceleration) acts in the opposite direction, thus suppressing the downward motion of the air. In contrast, above 1.5 km, both DA buoyancy and vertical velocity take positive values and therefore DAs enhance the upward air motion. In order to further assess the strength of the DA buoyancy with respect to the prevailing vertical velocities of the air, the change in the air vertical velocity induced by the DA buoyancy acting for 10 min is computed and is given in Figure S12. It is found that the dust buoyancy along the selected slant paths during the 3 days of the DAEC can cause a change in vertical velocity up to 8.6 m/s, which is of the same order of magnitude and comparable to the prevailing vertical velocities (up to 25.2 m/s, Figure 8). According to the obtained results, the buoyancy induced by DAs during intense dust transport events can partly explain and lead to the generally observed upward motions in and above the dust layers.

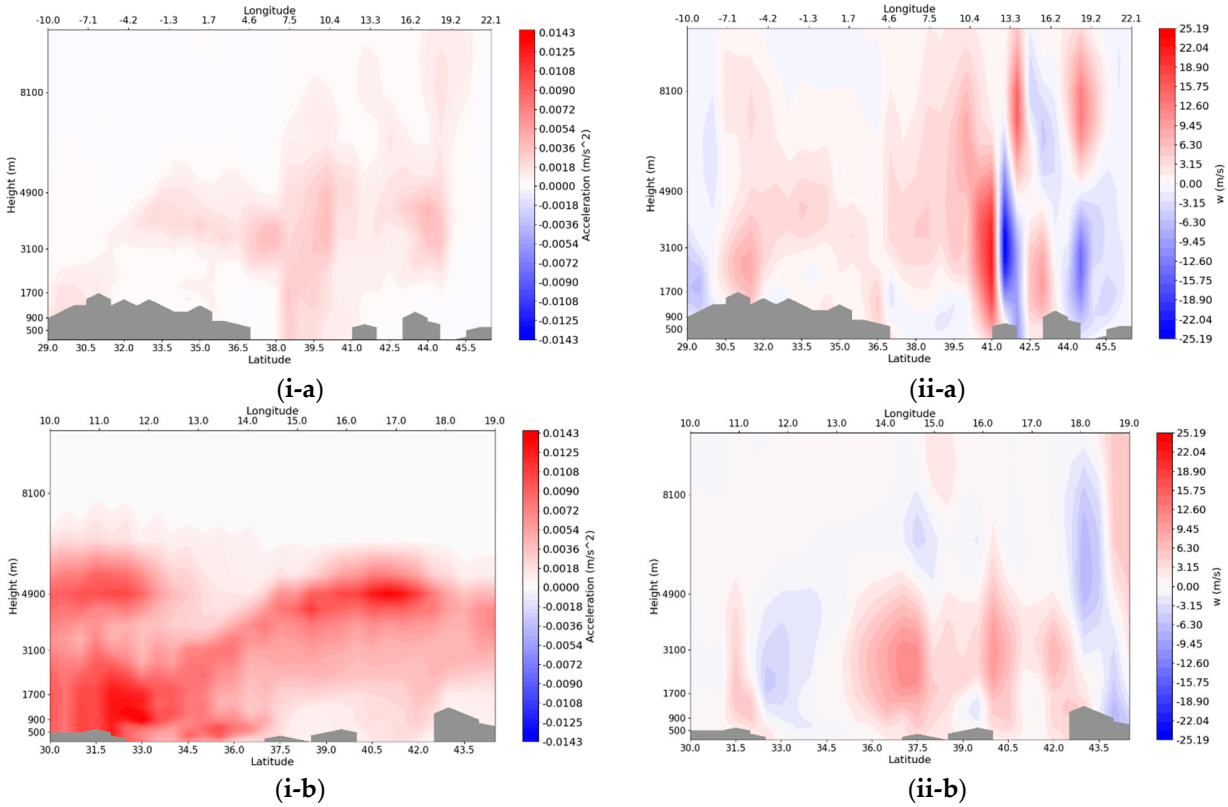

Figure 8. *Cont.*

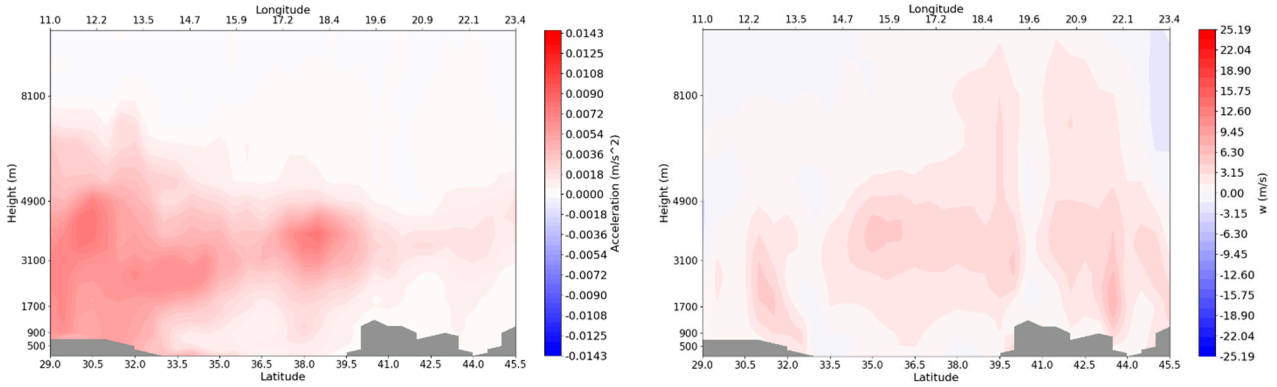

Figure 8. Vertical cross-sections of the buoyancy (vertical acceleration in m/s^2, (left column (**i**)) caused by dust aerosols, and the corresponding prevailing vertical wind speeds (in m/s, right column (**ii**)) along the slant path across the African dust export into the Mediterranean Basin (shown in Figure 5e, Figure 6e, and Figure 7e) during first (16 June 2016, (**a**)), second (17 June 2016, (**b**)), and third (18 June 2016, (**c**)) days of the dust episode that took place during 16–18 June 2016 over the Mediterranean Basin. The results are given at 12:00 UTC of each day.

3.5. Regional Mean DDREs

The dust radiative effects of the studied Mediterranean DAEC are also examined on a spatial mean basis. The spatial averaging is made over the part of the MB enclosed by the yellow frame (Figure 1), which includes the areas that are most affected by the dust export from the first (16 June 2016) until the last (third) day (18 June 2016) of the DAEC. The assessment of DDREs at a higher temporal resolution, specifically every 3 h, allows us to simultaneously follow the evolution of the regional mean DDREs at the TOA, in the atmosphere, and at the Earth's surface (they all refer to the absorbed solar radiation at these levels), as shown in Figure 9b. The timeseries of 3-hourly DDREs demonstrate the significant role of the available solar radiation for DDREs, since all DDREs follow the daily cycle of incoming solar radiation at the TOA, maximized at noon (Figure 9a). Thus, as shown in Figure 9b, the maximum perturbations of solar radiation at the TOA (up to -8 W/m^2 or 2%), in the atmosphere (up to +29 W/m^2 or 11%), and at the Earth's surface (down to -31 W/m^2 or 12%) are observed at 12:00 UTC, when the available solar radiation is also maximum (1250 W/m^2, Figure 9a). It should be noted that the corresponding regional mean DOD and SSA do not exhibit a considerable diurnal variation (Figure S9). In general, the maximum DDREs occur in the second day of the DAEC (17 June 2016), when the regional mean DOD is also maximum (0.26, Figure S13). Negative (down to -9 W/m^2) DDREs are estimated at the TOA, which means that the exported African dust produces a planetary cooling effect of the region, except for 12:00 UTC on the first day, when the TOA DDRE takes a small positive value (+1 W/m^2), indicating a slight planetary warning over the region. Although the DDREs in the atmosphere and at the Earth's surface are maximum at noon, the TOA DDREs follow a different diurnal cycle with minimum values at noon and larger values in the early morning (06:00 UTC) or in the afternoon (15:00 UTC). The same diurnal variation was also found by [45] who used the WRF-Chem model to investigate the radiative impact of an extreme dust episode that took place in February 2015 over the central and eastern MB. However, the magnitude of DDREs found in [45] is greater (magnitudes up to 35 W/m^2 in the atmosphere, 48 W/m^2 at the surface, and 17 W/m^2 at TOA) than in the present study, mainly due to the fact that estimations in the other study were made for clear-sky conditions, opposite to the real all-sky conditions (with cloud fractions up to 1) considered here. It is interesting that the estimated regional mean perturbation of the net surface solar radiation at 12:00 UTC associated with the examined African dust export (-31 W/m^2 on 17 June 2016) largely exceeds the corresponding mean monthly total DRE (caused by all aerosol types) being equal to -21 W/m^2 in June [55]. As

shown in Figure 9c, dust aerosols significantly perturb the regional solar radiation budget, by up to 12% at the surface, 11% in the atmosphere, and 2% at the TOA.

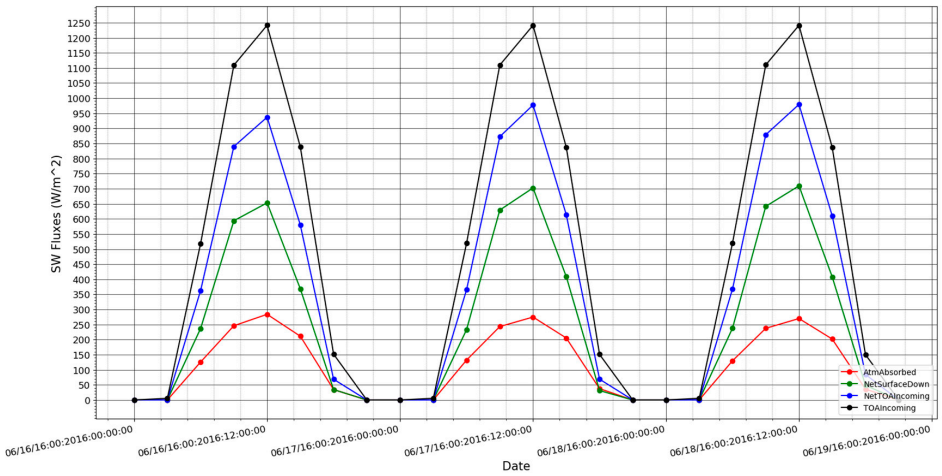

(**a**)

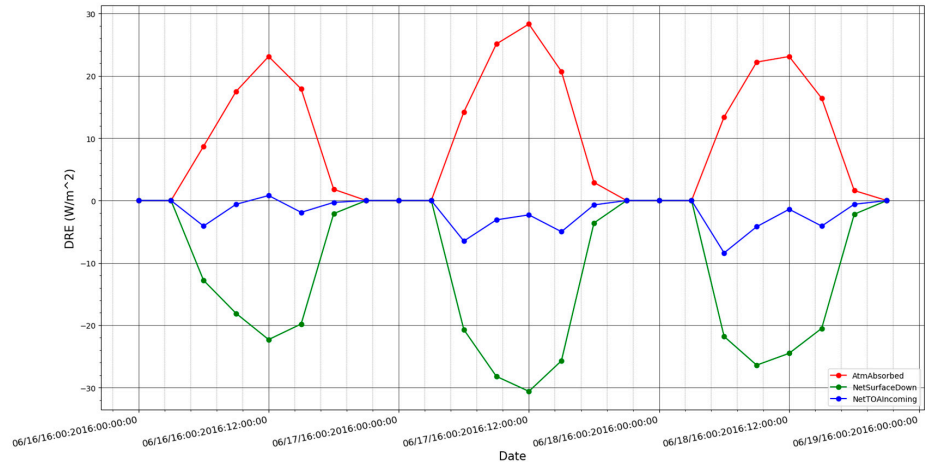

(**b**)

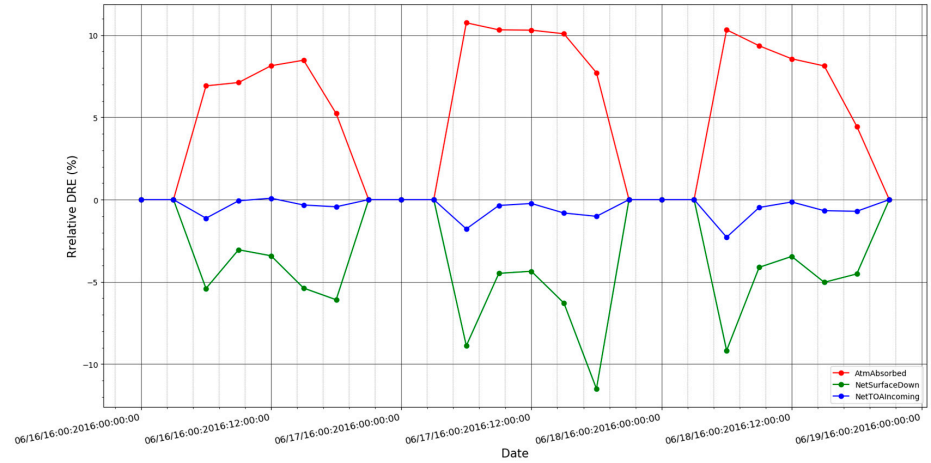

(**c**)

Figure 9. Time series of the 3-hourly spatial mean SW fluxes (**a**), dust DREs (in W/m^2) (**b**), and percent relative dust DREs with respect to the corresponding solar fluxes (**c**). All results refer to the solar radiation absorbed at the TOA (blue color), in the atmosphere (red), and at the Earth's surface (green color). The spatial averaging is performed over the Mediterranean areas affected by the African dust export (yellow frame of Figure 1).

4. Summary and Conclusions

In the present study, a new version of the spectral FORTH RTM, which is vertically resolved and takes into account 3-D distributions of aerosols and other atmospheric parameters, was run at high spatial ($0.5^\circ \times 0.625^\circ$) and temporal (3-hourly) resolution to investigate in detail the three-dimensional distributions of the SW direct radiative effect of an intense African dust episode (DAEC) that took place from 16 to 18 June 2016 over the central and eastern MB. The model ran under all-sky conditions accounting for analytical profiles of cloud and aerosol optical properties, using data from the satellite ISCCP-H and MERRA-2 reanalysis databases, respectively. Running with all aerosols, and all except for dust, the RTM estimated the SW fluxes at the TOA, in the atmosphere, at the Earth's surface, as well as at 50 levels in the atmosphere, and estimated from their difference the corresponding dust DREs (DDREs). The model fluxes at the TOA and at the Earth's surface were evaluated against satellite (CERES-SYNOP) and ground (BSRN) measurements, respectively. In addition, the model estimated the vertically resolved atmospheric heating rates induced by the dust absorption of solar radiation, i.e., the atmospheric SW DDRE, and also quantified their contribution to the modification of the atmospheric lapse rates, which exhibited reduced temperature gradients and temperature inversions over the Mediterranean areas affected by the African dust transport. Finally, the model quantified the buoyancy produced by the SW atmospheric DDRE, as well as the consequent modification of the vertical velocity, which is important for the mixing of energy and cloud formation. All these aspects of the present work offer an unprecedented highly spatially (horizontally and vertically) and temporally (3-hourly) resolved assessment of the direct SW radiative effects of dust under episodic conditions over the climatically sensitive Mediterranean Basin, regarded as a climate change hotspot. The main conclusions of the current study are summarized below.

- The RTM-estimated SW fluxes are reliable, giving confidence in the obtained DDREs. Specifically, during the 3 days of the examined DAEC (from 16 to 18 June 2016), the model fluxes at the TOA and at the Earth's surface compared well against CERES and BSRN data, respectively, achieving a reasonable closure of the SW radiation budget. The 3-hourly matched pairs yield overall correlation coefficients equal to 0.98 and 0.88, and relative biases equal to 0.8 and 3.5%, against CERES and BSRN, respectively. Based on this uncertainty of the RTM solar fluxes, the modeled DDREs have an uncertainty smaller than 7%.
- The model input MERRA-2 dust optical properties, in particular the optical depth, agrees reasonably well against reference data from AERONET stations located in areas affected by the transported African dust. MERRA-2 successfully reproduces the intra-daily variation in the dust aerosol loads, representing the spread of the dust outbreak over the central and eastern MB and its gradual eastward shift during the 3-day period (16–18 June 2016) of the examined DAEC.
- Dust aerosols cause a significant solar atmospheric radiative heating over areas undergoing the African dust export, extending from northern Africa to as far as the northern Balkans and the Black Sea. The SW atmospheric DDRE is maximum (values up to 187 W/m^2 at 12:00 UTC or 72 W/m^2 on a daily mean basis) over locations with the maximum dust loadings. Respectively, over these heavily dust loaded areas, DAs also induce a significant surface radiative cooling, with maximum values equal to 200 W/m^2 at 12:00 UTC and 62 W/m^2 on a daily mean basis. As a result of the atmospheric warming and surface cooling, a considerable planetary cooling is found over the areas of dust transport, as strong as -40 W/m^2 at 12:00 UTC, which turns to an appreciable planetary warming (up to 70 W/m^2) over highly reflecting African desert areas overloaded by dust.
- The above-mentioned SW DDREs significantly perturb the regional solar radiation budget, in particular over the Mediterranean areas undergoing the dust export, by up to 45% in the atmosphere and 35% at the surface, thus constituting an important factor for processes such as the modification of temperature or humidity, and for dynamical

effects, such as the creation of horizontal and vertical temperature gradients, leading to changes in air motions and local circulations.

- The vertical resolution of the obtained RTM results gives insight into the existence of strong differences in SW atmospheric DDREs with height. Thus, along the pathways of the dust export, and within the layers having the highest dust loadings found up to 5–6 km in height, the largest DDREs, up to about 13 W/m^2, are observed in the second day of the DAEC, namely on 17 June 2016, near 5 km. Apart from the significant vertical differences in magnitude, the model results reveal even a change in the sign of atmospheric DDREs, resulting in limited atmospheric cooling.
- The atmospheric solar radiative dust DREs cause a significant heating effect, producing heating rates up to 0.14 K/3 h on 17 June 2016, 12:00 UTC, being maximum within layers with the highest dust loadings, namely at heights between 3 and 5 km, but also with significant values down to the surface. Such important heating rates within air masses that carry dust loadings create significant horizontal and vertical temperature gradients, which can alter the distribution of isobars and induce horizontal pressure gradients with consequent effects on the dynamics of the regional atmosphere.
- The atmospheric heating induced by the absorption of solar radiation by DAs produces a buoyancy, with a maximum in the second day of the DAEC, which either favors or suppresses the vertical air motions, depending on the prevailing conditions. The vertical acceleration caused by dust aerosols was as large as 0.014 m/s^2 on 17 June 2016 at 12:00 UTC within the elevated dust layer, near 5–6 km. This dust-induced buoyancy produces significant modifications to the vertical air velocity. For example, according to the model results, should an acceleration equal to 0.014 m/s^2 persist for 10 min, the change in air velocity would be as large as 8.6 m/s, being of the same order of magnitude and comparable to the prevailing vertical velocities. Such modifications of vertical air motions due to dust can be related to the observed (e.g., [50]) effects on cloud formation, especially the high-level ones.

From the above-mentioned findings of this study, the most important ones are: (i) during intense spatially extended African dust exports, the SW radiative budget of the Mediterranean basin is significantly perturbed, by at least one order of magnitude than it does in background aerosol loading conditions, reaching hundreds of watts per square meter; (ii) the SW radiative perturbation induces significant radiative cooling at the surface and heating in the atmosphere of the areas affected by the dust export, thus creating temperature gradients with less- or non-affected areas; (iii) the dust-induced radiative cooling/heating along with the warm advection, which takes place during the transport of DAs from the hot desert areas of N. Africa to the MB, modify not only the region's atmospheric temperature structure, but also its stability, resulting in systematic intense temperature inversions and/or reduced temperature lapse rates below the elevated dust layer; this is reported for the first time for the Mediterranean Basin; (iv) yet, the interaction (absorption) of solar radiation with (by) dust is not the main driver for the formation of the atmospheric lapse rate during the DAEC, which may be driven by other mechanisms, such as the advection of heat or thermodynamic processes; (v) the effect of dust transport on buoyancy is investigated/quantified for the first time, showing that dust episodes induce an upward vertical acceleration of air masses, being strongest close to heights with the highest dust loadings, which can partly explain and lead to the generally observed upward motions in and above the dust layers.

The current RTM-based study is, to our knowledge, the first to provide such a detailed investigation of the SW DDREs during an intense summer dust episode over the MB. The obtained results complement those obtained in the past from very few other studies that were performed for other periods of the year, but also significantly extend them, providing insights into weather- and climate-relevant issues such as the dust-induced atmospheric heating rates and the produced buoyancy and modifications of vertical air velocity. The model results confirm the significant perturbation of the regional SW radiation budget and the modification of atmospheric temperature fields caused by Mediterranean dust

episodes, but also prove that the role of dust DREs in decreased temperature gradients and temperature inversions during such intense dust transport episodes is secondary to other factors such as the advection of heat. In the future, we plan to extend the present study, by also accounting for the dust effect on longwave radiation, which is smaller than the SW effect, but still considerable in the case of dust episodes. Additionally, the results of this study, such as the effects of DAs on temperature profiles, vertical air motions, and cloud formation, are planned to be elucidated in more detail and inter-compared with those obtained by simulations performed with the state-of-the-art WRF-Chem mesoscale model accounting for aerosol–cloud and aerosol–radiation interactions. Finally, a climatology of dust DREs will be created, based on 98 Mediterranean intense dust episodes, similarly to the one studied here, that took place from 2005 to 2019 [50], allowing the generalization of the present findings in terms of possible effects of dust episodes on the regional weather and climate.

Supplementary Materials: The following supporting information can be downloaded at: https://www.mdpi.com/article/10.3390/app13126878/s1, Figure S1: The geographical distribution of 31 AERONET stations in the wider Mediterranean area providing data during the DAEC period (16–18 June 2016) and used for the evaluation of the MERRA-2 aerosol optical depth and single scattering albedo; Figure S2: The geographical distribution of 7 BSRN stations in the wider Mediterranean area providing data during the DAEC period (16–18 June 2016). Their short names are shown along with their locations (pal: Palaiseau, pay: Payerne, car: Carpentras, son: Sonnblick, cnr: Cener, tam: Tamanrasset, iza: Izaña); Figure S3: (a) Scatter plot comparison between AOD550nm from MERRA-2 and AERONET, (b) Time-series of hourly AOD values averaged over the 31 Mediterranean AERONET stations (blue) and corresponding MERRA-2 AODs (red) from grids containing the AERONET sites; Figure S4: Scatter plot comparison between SSA of MERRA-2 and AERONET over the 8 stations during 16–18 June 2016; Figure S5: Scatter plot comparison between SSR fluxes (W/m^2) of FORTH RTM and BSRN (i-a) and OSR fluxes (W/m^2) of FORTH RTM and CERES (i-b). The different colors in (i-a) indicate the different (7, see Figure 1) stations and the statistical metrics and linear regression fit line are also shown. Also, (ii-a) shows the average (for the 7 stations) 3-hourly SSR fluxes (W/m^2) for FORTH RTM (red) and BSRN (blue) sites during 16–18 June 2016, while (ii-b) shows the 3-hourly average (for the entire study region) OSR fluxes (W/m^2) for FORTH (red) and CERES (blue) sites; Figure S6: Scatter plot comparison between OSR fluxes (W/m^2) of FORTH RTM and CERES (a) over the 7 BSRN stations during 16–18 June 2016. Also, (b) shows the average 3-hourly OSR fluxes (W/m^2) for FORTH RTM (red) and CERES (blue) over the BSRN sites; Figure S7: Geographical distribution of ISCCP-H cloud amount for liquid (left column) and ice (right column) phase clouds during the day before (first row, a), and the first (second row, b), second (third row, c), third (fourth row, d) and the day after (fifth row, e) the DAEC that took place during 16–18 June 2016 over the Mediterranean Basin. Results are given at 12:00 UTC of each day; Figure S8: Geographical distribution of ISCCP-H cloud top pressure in hPa (left column, i), cloud top temperature in K (middle column, ii) and cloud optical depth (right column, iii) during the day before (first row, a), and the first (second row, b), second (third row, c), third (fourth row, d) and the day after (fifth row, e) the DAEC that took place during 16–18 June 2016 over the Mediterranean Basin. Results are given at 12:00 UTC of each day; Figure S9: Geographical distribution of MERRA-2 SSA (left column) and AP (right column) during the day before (first row, a), the first (second row, b), the second (third row, c), the third (fourth row, d) and the day after (fifth row, e) of the dust episode that took place during 16–18 June 2016 over the Mediterranean Basin. Results are given at 12:00 UTC of each day; Figure S10: Ge-ographical dis-tribution of: the daily mean ab-sorbed solar ra-diation (in W/m^2) at the top of at-mosphere (left column, i), in the atmosphere middle column, ii) and at the Earths surface (right column, iii) for the first (first row, a), second (second row, b) and third (third row, c) day of the dust episode that took place during 16–18 June 2016 over the Medi-terranean Basin; Figure S11: Ge-ographical dis-tribution of the dust direct radi-ative effects ex-pressed in per-cent terms (%) of the correspond-ing radiative fluxes (consider-ing all aerosols), namely of the absorbed solar radiation: at the top of atmos-phere (left col-umn, i), in the atmosphere (middle column, ii) and at the Earths surface (right column, iii) for the first (first row, a), second (second row, b) and third (third row, c) day (at 12:00 UTC) of the dust episode that took place during 16–18 June 2016 over the Medi-terranean Basin; Figure S12: Vertical cross-sections of the change in vertical velocity (in m/s) should the DA induced buoyancy (shown

in Figure 8i-a,b,c) persist for 10 min, during the first day (a, 16 June 2016), second (b, 17 June 2016) and third (c, 18/06/2016) days of the dust episode that took place during 16–18 June 2016 over the Mediterranean Basin. The results are given along the slant paths across the African dust export into the Mediterranean Basin (shown on the map of DOD, Figures 5, 6 and 7e, respectively); Figure S13: Time series of the 3-hourly mean DOD (red line) and associated dust SSA (blue line) averaged over the Mediterranean areas (yellow frame in Figure 8) affected by the dust export during the DAEC from 16 to 18 June 2016.

Author Contributions: Conceptualization, N.H. and M.G.; methodology, N.H. and M.G.; software, M.G., M.-B.K.-C., C.M., I.V. and N.H.; formal analysis, M.G.; investigation, N.H. and M.G.; resources, N.H., M.G., M.-B.K.-C. and M.S.; data curation, N.H., M.G., M.-B.K.-C. and M.S.; writing—original draft preparation, M.G.; writing—review and editing, N.H., N.M., M.-B.K.-C., C.L., C.M., I.V., M.S. and M.G.; visualization, M.S. and M.G.; supervision, N.H.; project administration, N.H. All authors have read and agreed to the published version of the manuscript.

Funding: The research work was supported by the Hellenic Foundation for Research and Innovation (HFRI) under the 3rd Call for HFRI PhD Fellowships (Fellowship Number: 6353).

Institutional Review Board Statement: Not applicable.

Informed Consent Statement: Not applicable.

Data Availability Statement: The data presented in this study are available on request from the corresponding author.

Acknowledgments: Marios-Bruno Korras-Carraca was supported by the Hellenic Foundation for Research and Innovation (H.F.R.I.) under the "2nd Call for H.F.R.I. Research Projects to support Post-Doctoral Researchers" (project acronym: ATLANTAS, project no. 544). Michalis Stamatis was supported by the project "Dioni: Computing Infrastructure for Big-Data Processing and Analysis." (MIS No. 5047222) which is implemented under the Action "Reinforcement of the Research and Innovation Infrastructure", funded by the Operational Programme "Competitiveness, Entrepreneurship and Innovation" (NSRF 2014–2020) and co-financed by Greece and the European Union (European Regional Development Fund).

Conflicts of Interest: The authors declare no conflict of interest.

References

1. Cakmur, R.; Miller, R.; Perlwitz, J.; Geogdzhayev, I.; Ginoux, P.; Koch, D.; Kohfeld, K.; Tegen, I.; Zender, C. Constraining the Magnitude of the Global Dust Cycle by Minimizing the Difference between a Model and Observations. *J. Geophys. Res. Atmos.* **2006**, *111*, D06207. [CrossRef]
2. Yin, Y.; Wurzler, S.; Levin, Z.; Reisin, T.G. Interactions of Mineral Dust Particles and Clouds: Effects on Precipitation and Cloud Optical Properties. *J. Geophys. Res. Atmos.* **2002**, *107*, AAC-19. [CrossRef]
3. Sokolik, I.N.; Winker, D.; Bergametti, G.; Gillette, D.; Carmichael, G.; Kaufman, Y.; Gomes, L.; Schuetz, L.; Penner, J. Introduction to Special Section: Outstanding Problems in Quantifying the Radiative Impacts of Mineral Dust. *J. Geophys. Res. Atmos.* **2001**, *106*, 18015–18027. [CrossRef]
4. Heinold, B.; Tegen, I.; Schepanski, K.; Hellmuth, O. Dust Radiative Feedback on Saharan Boundary Layer Dynamics and Dust Mobilization. *Geophys. Res. Lett.* **2008**, *35*, L20817. [CrossRef]
5. Korras-Carraca, M.-B.; Gkikas, A.; Matsoukas, C.; Hatzianastassiou, N. Global Clear-Sky Aerosol Speciated Direct Radiative Effects over 40 Years (1980–2019). *Atmosphere* **2021**, *12*, 1254. [CrossRef]
6. Di Sarra, A.; Di Biagio, C.; Meloni, D.; Monteleone, F.; Pace, G.; Pugnaghi, S.; Sferlazzo, D. Shortwave and Longwave Radiative Effects of the Intense Saharan Dust Event of 25–26 March 2010 at Lampedusa (Mediterranean Sea). *J. Geophys. Res. Atmos.* **2011**, *116*, D23209. [CrossRef]
7. Nabat, P.; Somot, S.; Mallet, M.; Michou, M.; Sevault, F.; Driouech, F.; Meloni, D.; Di Sarra, A.; Di Biagio, C.; Formenti, P. Dust Aerosol Radiative Effects during Summer 2012 Simulated with a Coupled Regional Aerosol–Atmosphere–Ocean Model over the Mediterranean. *Atmos. Chem. Phys.* **2015**, *15*, 3303–3326. [CrossRef]
8. Gkikas, A.; Obiso, V.; Perez Garcia-Pando, C.; Jorba, O.; Hatzianastassiou, N.; Vendrell, L.; Basart, S.; Solomos, S.; Gassó, S.; Baldasano, J.M. Direct Radiative Effects during Intense Mediterranean Desert Dust Outbreaks. *Atmos. Chem. Phys.* **2018**, *18*, 8757–8787. [CrossRef]
9. Mallet, M.; Pont, V.; Liousse, C.; Gomes, L.; Pelon, J.; Osborne, S.; Haywood, J.; Roger, J.-C.; Dubuisson, P.; Mariscal, A. Aerosol Direct Radiative Forcing over Djougou (Northern Benin) during the African Monsoon Multidisciplinary Analysis Dry Season Experiment (Special Observation Period-0). *J. Geophys. Res. Atmos.* **2008**, *113*, D00C01. [CrossRef]

10. Roger, J.-C.; Mallet, M.; Dubuisson, P.; Cachier, H.; Vermote, E.; Dubovik, O.; Despiau, S. A Synergetic Approach for Estimating the Local Direct Aerosol Forcing: Application to an Urban Zone during the Expérience Sur Site Pour Contraindre Les Modèles de Pollution et de Transport d'Emission (ESCOMPTE) Experiment. *J. Geophys. Res. Atmos.* **2006**, *111*, D13208. [CrossRef]
11. Sicard, M.; Mallet, M.; García-Vizcaíno, D.; Comerón, A.; Rocadenbosch, F.; Dubuisson, P.; Muñoz-Porcar, C. Intense Dust and Extremely Fresh Biomass Burning Outbreak in Barcelona, Spain: Characterization of Their Optical Properties and Estimation of Their Direct Radiative Forcing. *Environ. Res. Lett.* **2012**, *7*, 034016. [CrossRef]
12. Ryder, C.; Highwood, E.; Lai, T.; Sodemann, H.; Marsham, J.H. Impact of Atmospheric Transport on the Evolution of Microphysical and Optical Properties of Saharan Dust. *Geophys. Res. Lett.* **2013**, *40*, 2433–2438. [CrossRef]
13. Sicard, M.; Bertolín, S.; Mallet, M.; Dubuisson, P.; Comerón, A. Estimation of Mineral Dust Long-Wave Radiative Forcing: Sensitivity Study to Particle Properties and Application to Real Cases in the Region of Barcelona. *Atmos. Chem. Phys.* **2014**, *14*, 9213–9231. [CrossRef]
14. Ansmann, A.; Tesche, M.; Seifert, P.; Althausen, D.; Engelmann, R.; Fruntke, J.; Wandinger, U.; Mattis, I.; Müller, D. Evolution of the Ice Phase in Tropical Altocumulus: SAMUM Lidar Observations over Cape Verde. *J. Geophys. Res. Atmos.* **2009**, *114*, D17208. [CrossRef]
15. Niedermeier, D.; Hartmann, S.; Shaw, R.; Covert, D.; Mentel, T.; Schneider, J.; Poulain, L.; Reitz, P.; Spindler, C.; Clauss, T. Heterogeneous Freezing of Droplets with Immersed Mineral Dust Particles–Measurements and Parameterization. *Atmos. Chem. Phys.* **2010**, *10*, 3601–3614. [CrossRef]
16. Seinfeld, J.H.; Bretherton, C.; Carslaw, K.S.; Coe, H.; DeMott, P.J.; Dunlea, E.J.; Feingold, G.; Ghan, S.; Guenther, A.B.; Kahn, R. Improving Our Fundamental Understanding of the Role of Aerosol—Cloud Interactions in the Climate System. *Proc. Natl. Acad. Sci. USA* **2016**, *113*, 5781–5790. [CrossRef]
17. Schepanski, K. Transport of Mineral Dust and Its Impact on Climate. *Geosciences* **2018**, *8*, 151. [CrossRef]
18. Li, W.; Shao, L. Transmission Electron Microscopy Study of Aerosol Particles from the Brown Hazes in Northern China. *J. Geophys. Res. Atmos.* **2009**, *114*, D09302. [CrossRef]
19. Matsuki, A.; Schwarzenboeck, A.; Venzac, H.; Laj, P.; Crumeyrolle, S.; Gomes, L. Cloud Processing of Mineral Dust: Direct Comparison of Cloud Residual and Clear Sky Particles during AMMA Aircraft Campaign in Summer 2006. *Atmos. Chem. Phys.* **2010**, *10*, 1057–1069. [CrossRef]
20. Nenes, A.; Murray, B.; Bougiatioti, A. Mineral Dust and Its Microphysical Interactions with Clouds. In *Mineral Dust*; Springer: Berlin/Heidelberg, Germany, 2014; pp. 287–325.
21. Marinou, E.; Voudouri, K.A.; Tsikoudi, I.; Drakaki, E.; Tsekeri, A.; Rosoldi, M.; Ene, D.; Baars, H.; O'Connor, E.; Amiridis, V. Geometrical and Microphysical Properties of Clouds Formed in the Presence of Dust above the Eastern Mediterranean. *Remote Sens.* **2021**, *13*, 5001. [CrossRef]
22. Twomey, S. The Influence of Pollution on the Shortwave Albedo of Clouds. *J. Atmos. Sci.* **1977**, *34*, 1149–1152. [CrossRef]
23. Rosenfeld, D.; Rudich, Y.; Lahav, R. Desert Dust Suppressing Precipitation: A Possible Desertification Feedback Loop. *Proc. Natl. Acad. Sci. USA* **2001**, *98*, 5975–5980. [CrossRef] [PubMed]
24. Cheng, W.; Carrio, G.; Cotton, W.; Saleeby, S. Influence of Atmospheric Aerosols on the Development of Precipitating Trade Wind Cumuli in a Large Eddy Simulation. *J. Geophys. Res* **2009**, *114*, D08201. [CrossRef]
25. Levin, Z.; Cotton, W.R. *Aerosol Pollution Impact on Precipitation: A Scientific Review*; Springer Science & Business Media: Berlin/Heidelberg, Germany, 2008.
26. Andreae, M.O.; Rosenfeld, D.; Artaxo, P.; Costa, A.; Frank, G.; Longo, K.; Silva-Dias, M.A.F.d. Smoking Rain Clouds over the Amazon. *Science* **2004**, *303*, 1337–1342. [CrossRef]
27. Huang, C.-C.; Chen, S.-H.; Lin, Y.-C.; Earl, K.; Matsui, T.; Lee, H.-H.; Tsai, I.-C.; Chen, J.-P.; Cheng, C.-T. Impacts of Dust–Radiation versus Dust–Cloud Interactions on the Development of a Modeled Mesoscale Convective System over North Africa. *Mon. Weather Rev.* **2019**, *147*, 3301–3326. [CrossRef]
28. Jia, G.; Shevliakova, E.; Artaxo, P.; De-Docoudré, N.; Houghton, R.; House, J.; Kitajima, K.; Lennard, C.; Popp, A.; Sirin, A.; et al. Land–Climate interactions. In *Special Report on Climate Change and Land: An Ipcc Special Report on Climate Change, Desertification, Land Degradation, Sustainable Land Management, Food Security, and Greenhouse Gas Fluxes in Terrestrial Ecosystems*; IPCC: Geneva, Switzerland, 2019; pp. 133–206.
29. Bullard, J.E.; Baddock, M.; Bradwell, T.; Crusius, J.; Darlington, E.; Gaiero, D.; Gassó, S.; Gisladottir, G.; Hodgkins, R.; McCulloch, R. High-latitude Dust in the Earth System. *Rev. Geophys.* **2016**, *54*, 447–485. [CrossRef]
30. Prospero, J.M.; Bullard, J.E.; Hodgkins, R. High-Latitude Dust over the North Atlantic: Inputs from Icelandic Proglacial Dust Storms. *Science* **2012**, *335*, 1078–1082. [CrossRef]
31. Engelstaedter, S.; Tegen, I.; Washington, R. North African Dust Emissions and Transport. *Earth-Sci. Rev.* **2006**, *79*, 73–100. [CrossRef]
32. Ginoux, P.; Prospero, J.M.; Gill, T.E.; Hsu, N.C.; Zhao, M. Global-scale Attribution of Anthropogenic and Natural Dust Sources and Their Emission Rates Based on MODIS Deep Blue Aerosol Products. *Rev. Geophys.* **2012**, *50*, RG3005. [CrossRef]
33. Gavrouzou, M.; Hatzianastassiou, N.; Gkikas, A.; Korras-Carraca, M.-B.; Mihalopoulos, N. A Global Climatology of Dust Aerosols Based on Satellite Data: Spatial, Seasonal and Inter-Annual Patterns over the Period 2005–2019. *Remote Sens.* **2021**, *13*, 359. [CrossRef]

34. Yoon, J.-E.; Lim, J.-H.; Shim, J.-M.; Kwon, J.-I.; Kim, I.-N. Spring 2018 Asian Dust Events: Sources, Transportation, and Potential Biogeochemical Implications. *Atmosphere* **2019**, *10*, 276. [CrossRef]
35. Evan, A.T.; Mukhopadhyay, S. Optical Depth of Atlantic Dust as NetCDF Files. Supplement to: Evan, AT; Mukhopadhyay, S (2010): African dust over the Northern Tropical Atlantic: 1955–2008. *J. Appl. Meteorol. Climatol.* **2010**, *49*, 2213–2229. [CrossRef]
36. Velasco-Merino, C.; Mateos, D.; Toledano, C.; Prospero, J.M.; Molinie, J.; Euphrasie-Clotilde, L.; González, R.; Cachorro, V.E.; Calle, A.; de Frutos, A.M. Impact of Long-Range Transport over the Atlantic Ocean on Saharan Dust Optical and Microphysical Properties Based on AERONET Data. *Atmos. Chem. Phys.* **2018**, *18*, 9411–9424. [CrossRef]
37. Wang, K.; Liu, C. Transport of the Saharan Dust Air Plumes over the Tropical North Atlantic from FORMOSAT–3/COSMIC Observation. *Atmos. Pollut. Res.* **2014**, *5*, 539–553. [CrossRef]
38. Aklesso, M.; Kumar, K.R.; Bu, L.; Boiyo, R. Analysis of Spatial-Temporal Heterogeneity in Remotely Sensed Aerosol Properties Observed during 2005–2015 over Three Countries along the Gulf of Guinea Coast in Southern West Africa. *Atmos. Environ.* **2018**, *182*, 313–324. [CrossRef]
39. Gavrouzou, M.; Hatzianastassiou, N.; Gkikas, A.; Lolis, C.J.; Mihalopoulos, N. A Climatological Assessment of Intense Desert Dust Episodes over the Broader Mediterranean Basin Based on Satellite Data. *Remote Sens.* **2021**, *13*, 2895. [CrossRef]
40. Gkikas, A.; Basart, S.; Hatzianastassiou, N.; Marinou, E.; Amiridis, V.; Kazadzis, S.; Pey, J.; Querol, X.; Jorba, O.; Gassó, S. Mediterranean Intense Desert Dust Outbreaks and Their Vertical Structure Based on Remote Sensing Data. *Atmos. Chem. Phys.* **2016**, *16*, 8609–8642. [CrossRef]
41. Papadimas, C.; Hatzianastassiou, N.; Mihalopoulos, N.; Querol, X.; Vardavas, I. Spatial and Temporal Variability in Aerosol Properties over the Mediterranean Basin Based on 6-year (2000–2006) MODIS Data. *J. Geophys. Res. Atmos.* **2008**, *113*, D11205. [CrossRef]
42. Schepanski, K.; Mallet, M.; Heinold, B.; Ulrich, M. North African Dust Transport toward the Western Mediterranean Basin: Atmospheric Controls on Dust Source Activation and Transport Pathways during June–July 2013. *Atmos. Chem. Phys.* **2016**, *16*, 14147–14168. [CrossRef]
43. Solomos, S.; Kalivitis, N.; Mihalopoulos, N.; Amiridis, V.; Kouvarakis, G.; Gkikas, A.; Binietoglou, I.; Tsekeri, A.; Kazadzis, S.; Kottas, M. From Tropospheric Folding to Khamsin and Foehn Winds: How Atmospheric Dynamics Advanced a Record-Breaking Dust Episode in Crete. *Atmosphere* **2018**, *9*, 240. [CrossRef]
44. Gkikas, A.; Houssos, E.; Lolis, C.; Bartzokas, A.; Mihalopoulos, N.; Hatzianastassiou, N. Atmospheric Circulation Evolution Related to Desert-dust Episodes over the Mediterranean. *Q. J. R. Meteorol. Soc.* **2015**, *141*, 1634–1645. [CrossRef]
45. Gkikas, A.; Giannaros, T.; Kotroni, V.; Lagouvardos, K. Assessing the Radiative Impacts of an Extreme Desert Dust Outbreak and the Potential Improvements on Short-Term Weather Forecasts: The Case of February 2015. *Atmos. Res.* **2019**, *226*, 152–170. [CrossRef]
46. Meloni, D.; Di Sarra, A.; Di Iorio, T.; Fiocco, G. Influence of the Vertical Profile of Saharan Dust on the Visible Direct Radiative Forcing. *J. Quant. Spectrosc. Radiat. Transf.* **2005**, *93*, 397–413. [CrossRef]
47. Bangert, M.; Nenes, A.; Vogel, B.; Vogel, H.; Barahona, D.; Karydis, V.; Kumar, P.; Kottmeier, C.; Blahak, U. Saharan Dust Event Impacts on Cloud Formation and Radiation over Western Europe. *Atmos. Chem. Phys.* **2012**, *12*, 4045–4063. [CrossRef]
48. Gong, X.; Wex, H.; Müller, T.; Wiedensohler, A.; Höhler, K.; Kandler, K.; Ma, N.; Dietel, B.; Schiebel, T.; Möhler, O. Characterization of Aerosol Properties at Cyprus, Focusing on Cloud Condensation Nuclei and Ice-Nucleating Particles. *Atmos. Chem. Phys.* **2019**, *19*, 10883–10900. [CrossRef]
49. Tsarpalis, K.; Katsafados, P.; Papadopoulos, A.; Mihalopoulos, N. Assessing Desert Dust Indirect Effects on Cloud Microphysics through a Cloud Nucleation Scheme: A Case Study over the Western Mediterranean. *Remote Sens.* **2020**, *12*, 3473. [CrossRef]
50. Gavrouzou, M.; Hatzianastassiou, N.; Lolis, C.J.; Korras-Carraca, M.-B.; Mihalopoulos, N. Modification of Temperature Lapse Rates and Cloud Properties during a Spatiotemporally Extended Dust Aerosol Episode (16–18 June 2016) over the Mediterranean Basin Based on Satellite and Reanalysis Data. *Remote Sens.* **2022**, *14*, 679. [CrossRef]
51. Hatzianastassiou, N.; Matsoukas, C.; Drakakis, E.; Stackhouse, P., Jr.; Koepke, P.; Fotiadi, A.; Pavlakis, K.; Vardavas, I. The Direct Effect of Aerosols on Solar Radiation Based on Satellite Observations, Reanalysis Datasets, and Spectral Aerosol Optical Properties from Global Aerosol Data Set (GADS). *Atmos. Chem. Phys.* **2007**, *7*, 2585–2599. [CrossRef]
52. Vardavas, I.; Carver, J.H. Solar and Terrestrial Parameterizations for Radiative-Convective Models. *Planet. Space Sci.* **1984**, *32*, 1307–1325. [CrossRef]
53. Benas, N.; Hatzianastassiou, N.; Matsoukas, C.; Fotiadi, A.; Mihalopoulos, N.; Vardavas, I. Aerosol Shortwave Direct Radiative Effect and Forcing Based on MODIS Level 2 Data in the Eastern Mediterranean (Crete). *Atmos. Chem. Phys.* **2011**, *11*, 12647–12662. [CrossRef]
54. Granados-Muñoz, M.J.; Sicard, M.; Román, R.; Benavent-Oltra, J.A.; Barragán, R.; Brogniez, G.; Denjean, C.; Mallet, M.; Formenti, P.; Torres, B. Impact of Mineral Dust on Shortwave and Longwave Radiation: Evaluation of Different Vertically Resolved Parameterizations in 1-D Radiative Transfer Computations. *Atmos. Chem. Phys.* **2019**, *19*, 523–542. [CrossRef]
55. Papadimas, C.; Hatzianastassiou, N.; Matsoukas, C.; Kanakidou, M.; Mihalopoulos, N.; Vardavas, I. The Direct Effect of Aerosols on Solar Radiation over the Broader Mediterranean Basin. *Atmos. Chem. Phys.* **2012**, *12*, 7165–7185. [CrossRef]
56. Kosmopoulos, P.G.; Kazadzis, S.; Taylor, M.; Athanasopoulou, E.; Speyer, O.; Raptis, P.I.; Marinou, E.; Proestakis, E.; Solomos, S.; Gerasopoulos, E. Dust Impact on Surface Solar Irradiance Assessed with Model Simulations, Satellite Observations and Ground-Based Measurements. *Atmos. Meas. Tech.* **2017**, *10*, 2435–2453. [CrossRef]

57. Randles, C.A.; Kinne, S.; Myhre, G.; Schulz, M.; Stier, P.; Fischer, J.; Doppler, L.; Highwood, E.; Ryder, C.; Harris, B. Intercomparison of Shortwave Radiative Transfer Schemes in Global Aerosol Modeling: Results from the AeroCom Radiative Transfer Experiment. *Atmos. Chem. Phys.* **2013**, *13*, 2347–2379. [CrossRef]
58. Holben, B.N.; Eck, T.F.; al Slutsker, I.; Tanré, D.; Buis, J.; Setzer, A.; Vermote, E.; Reagan, J.A.; Kaufman, Y.; Nakajima, T. AERONET—A Federated Instrument Network and Data Archive for Aerosol Characterization. *Remote Sens. Environ.* **1998**, *66*, 1–16. [CrossRef]
59. Wild, M.; Folini, D.; Schär, C.; Loeb, N.; Dutton, E.; König-Langlo, G. *Basic Measurements of Radiation from the Baseline Surface Radiation Network (BSRN) in the Years 1992 to 2012, Reference List of 6378 Datasets*; PANGAEA: Bremen, Germany. [CrossRef]
60. Kotarba, A.Z. Evaluation of ISCCP Cloud Amount with MODIS Observations. *Atmos. Res.* **2015**, *153*, 310–317. [CrossRef]
61. Jones, P.W. First-and Second-Order Conservative Remapping Schemes for Grids in Spherical Coordinates. *Mon. Weather Rev.* **1999**, *127*, 2204–2210. [CrossRef]
62. Gelaro, R.; McCarty, W.; Suárez, M.J.; Todling, R.; Molod, A.; Takacs, L.; Randles, C.A.; Darmenov, A.; Bosilovich, M.G.; Reichle, R. The Modern-Era Retrospective Analysis for Research and Applications, Version 2 (MERRA-2). *J. Clim.* **2017**, *30*, 5419–5454. [CrossRef]
63. Buchard, V.; Randles, C.; Da Silva, A.; Darmenov, A.; Colarco, P.; Govindaraju, R.; Ferrare, R.; Hair, J.; Beyersdorf, A.; Ziemba, L. The MERRA-2 Aerosol Reanalysis, 1980 Onward. Part II: Evaluation and Case Studies. *J. Clim.* **2017**, *30*, 6851–6872. [CrossRef]
64. Shi, H.; Xiao, Z.; Zhan, X.; Ma, H.; Tian, X. Evaluation of MODIS and Two Reanalysis Aerosol Optical Depth Products over AERONET Sites. *Atmos. Res.* **2019**, *220*, 75–80. [CrossRef]
65. Hatzianastassiou, N.; Fotiadi, A.; Matsoukas, C.; Pavlakis, K.; Drakakis, E.; Hatzidimitriou, D.; Vardavas, I. Long-Term Global Distribution of Earth's Shortwave Radiation Budget at the Top of Atmosphere. *Atmos. Chem. Phys.* **2004**, *4*, 1217–1235. [CrossRef]
66. Korras-Carraca, M.; Pappas, V.; Hatzianastassiou, N.; Vardavas, I.; Matsoukas, C. Global Vertically Resolved Aerosol Direct Radiation Effect from Three Years of CALIOP Data Using the FORTH Radiation Transfer Model. *Atmos. Res.* **2019**, *224*, 138–156. [CrossRef]
67. Matsoukas, C.; Hatzianastassiou, N.; Fotiadi, A.; Pavlakis, K.; Vardavas, I. The Effect of Arctic Sea-Ice Extent on the Absorbed (Net) Solar Flux at the Surface, Based on ISCCP-D2 Cloud Data for 1983–2007. *Atmos. Chem. Phys.* **2010**, *10*, 777–787. [CrossRef]
68. Pyrina, M.; Hatzianastassiou, N.; Matsoukas, C.; Fotiadi, A.; Papadimas, C.; Pavlakis, K.; Vardavas, I. Cloud Effects on the Solar and Thermal Radiation Budgets of the Mediterranean Basin. *Atmos. Res.* **2015**, *152*, 14–28. [CrossRef]
69. Hatzianastassiou, N.; Papadimas, C.; Matsoukas, C.; Pavlakis, K.; Fotiadi, A.; Wild, M.; Vardavas, I. Recent Regional Surface Solar Radiation Dimming and Brightening Patterns: Inter-hemispherical Asymmetry and a Dimming in the Southern Hemisphere. *Atmos. Sci. Lett.* **2012**, *13*, 43–48. [CrossRef]
70. Hatzianastassiou, N.; Ioannidis, E.; Korras-Carraca, M.-B.; Gavrouzou, M.; Papadimas, C.D.; Matsoukas, C.; Benas, N.; Fotiadi, A.; Wild, M.; Vardavas, I. Global Dimming and Brightening Features during the First Decade of the 21st Century. *Atmosphere* **2020**, *11*, 308. [CrossRef]
71. Gueymard, C.A. The Sun's Total and Spectral Irradiance for Solar Energy Applications and Solar Radiation Models. *Sol. Energy* **2004**, *76*, 423–453. [CrossRef]
72. Joseph, J.H.; Wiscombe, W.; Weinman, J. The Delta-Eddington Approximation for Radiative Flux Transfer. *J. Atmos. Sci.* **1976**, *33*, 2452–2459. [CrossRef]
73. Tzallas, V.; Hatzianastassiou, N.; Benas, N.; Meirink, J.F.; Matsoukas, C.; Stackhouse, P.; Vardavas, I. Evaluation of CLARA-A2 and ISCCP-H Cloud Cover Climate Data Records over Europe with ECA & D Ground-Based Measurements. *Remote Sens.* **2019**, *11*, 212. [CrossRef]
74. Masmoudi, M.; Alfaro, S.C.; El Metwally, M. A Comparison of the Physical Properties of Desert Dust Retrieved from the Sunphotometer Observation of Major Events in the Sahara, Sahel, and Arabian Peninsula. *Atmos. Res.* **2015**, *158*, 24–35. [CrossRef]
75. Chen, T.; Rossow, W.B.; Zhang, Y. Radiative Effects of Cloud-Type Variations. *J. Clim.* **2000**, *13*, 264–286. [CrossRef]
76. Chand, D.; Wood, R.; Anderson, T.; Satheesh, S.; Charlson, R. Satellite-Derived Direct Radiative Effect of Aerosols Dependent on Cloud Cover. *Nat. Geosci.* **2009**, *2*, 181–184. [CrossRef]
77. Ramaswamy, V.; Freidenreich, S. A High-spectral Resolution Study of the Near-infrared Solar Flux Disposition in Clear and Overcast Atmospheres. *J. Geophys. Res. Atmos.* **1998**, *103*, 23255–23273. [CrossRef]
78. Nabat, P.; Solmon, F.; Mallet, M.; Kok, J.; Somot, S. Dust Emission Size Distribution Impact on Aerosol Budget and Radiative Forcing over the Mediterranean Region: A Regional Climate Model Approach. *Atmos. Chem. Phys.* **2012**, *12*, 10545–10567. [CrossRef]
79. Kacenelenbogen, M.S.; Vaughan, M.A.; Redemann, J.; Young, S.A.; Liu, Z.; Hu, Y.; Omar, A.H.; LeBlanc, S.; Shinozuka, Y.; Livingston, J. Estimations of Global Shortwave Direct Aerosol Radiative Effects above Opaque Water Clouds Using a Combination of A-Train Satellite Sensors. *Atmos. Chem. Phys.* **2019**, *19*, 4933–4962. [CrossRef]
80. Oikawa, E.; Nakajima, T.; Winker, D. An Evaluation of the Shortwave Direct Aerosol Radiative Forcing Using CALIOP and MODIS Observations. *J. Geophys. Res. Atmos.* **2018**, *123*, 1211–1233. [CrossRef]
81. Mishra, A.K.; Koren, I.; Rudich, Y. Effect of Aerosol Vertical Distribution on Aerosol-Radiation Interaction: A Theoretical Prospect. *Heliyon* **2015**, *1*, e00036. [CrossRef]

82. Meng, L.; Zhao, T.; He, Q.; Yang, X.; Mamtimin, A.; Wang, M.; Pan, H.; Huo, W.; Yang, F.; Zhou, C. Dust Radiative Effect Characteristics during a Typical Springtime Dust Storm with Persistent Floating Dust in the Tarim Basin, Northwest China. *Remote Sens.* **2022**, *14*, 1167. [CrossRef]
83. Choobari, O.A.; Zawar-Reza, P.; Sturman, A. Feedback between Windblown Dust and Planetary Boundary-Layer Characteristics: Sensitivity to Boundary and Surface Layer Parameterizations. *Atmos. Environ.* **2012**, *61*, 294–304. [CrossRef]
84. Yang, S.; Wang, Z.; Huang, X.; Wang, W.; Sheng, L.; Zhou, Y. Meteorological Feedback and Eco-Environmental Impact of Asian Dust: A Simulation Study. *Atmos. Environ.* **2021**, *253*, 118350. [CrossRef]